

# The CMB Power Spectrum: A Computational Investigation of the History of the Universe

L. E. Hansen<sup>1</sup>

Institute of Theoretical Astrophysics, University of Oslo, 0315 Oslo, Norway  
e-mail: l.e.hansen@fys.uio.no  
<https://github.com/leahelha/AST5220>

## ABSTRACT

This study investigates fundamental cosmological epochs and processes, in order to understand and reproduce the CMB power spectrum. Our fiducial cosmology was based off of Planck 2018 parameter constraints, but we neglected the contribution of neutrinos and polarization. The aim of this investigation is to enhance our understanding of the CMB and the evolution of our Universe, through numerical reproduction of the angular power spectrum of the CMB and the matter power spectrum. We attempted to reach our goal with a numerical model based on theoretical knowledge. The main methods we employed were numerical integration and close to direct implementations of functions from theory. In the early stage of our investigation we also evaluated our model based on an MCMC fit of the parameters  $\Omega_{k0}$ ,  $\Omega_{m0}$  and  $h$  made to fit supernova observations. We then analyzed the transitions and phenomena that shape the early Universe's evolution. Our analysis finds the times of the radiation-matter equality to be  $t = 2.32 \cdot 10^4$  years, the matter-dark energy equality to be 10.38 Gyrs, the recombination time to be 0.4085 Myr and the time of universe expansion acceleration to be 7.756 Gyrs. In computing the recombination we used the Saha approximation and Peebles equation to solve for when the electron fraction  $X_e < 0.1$ . We also computed the evolution of the density and velocities of perturbations in radiation and matter over time and for different scales,  $k$  in Fourier space, as well as the multipoles of the CMB temperature. In the end we arrived at a complete angular power spectrum and a matter power spectrum.

Despite having made some simplifications, we were able to reproduce the CMB angular power spectrum and the matter power spectrum to a degree of detail which still preserved many of the important features the two spectra contain. Such as the Sachs-Wolfe plateau, baryon loading, acoustic oscillations the and damping tail for the CMB power spectrum, and the characteristic shape of the matter power spectrum.

**Key words.** cosmic microwave background – large-scale structure of universe

## 1. Introduction

The Cosmic Microwave Background (CMB) radiation provides a window into the early universe, carrying with it information from a time shortly after the Big Bang. Understanding the CMB's power spectrum, allows us to read the chronological description of major events in the evolution of the universe through our understanding of the physics behind it. With modern advancements in observational technologies and computational methods that have allowed for increasingly precise measurements and simulations of the CMB power spectrum, like those made by WMAP Page et al. (2007), COBE Reichardt et al. (2009), and Planck Aghanim et al. (2020), the story we read becomes increasingly detailed.

This investigation attempts to explore the detailed characteristics of the CMB and to gain an understanding of the fundamental physics that govern cosmic evolution. Our approach involves computational simulations, where we attempt to model the evolution of the cosmic background geometry and constituents of the universe; matter, radiation and dark energy.

We will start our numerical investigation by first computing the background geometry of the universe. In this process we will evolve the density parameters  $\Omega_i$  for all the constituents, the conformal Hubble parameter,  $\mathcal{H}$ , and follow their evolution through cosmic time,  $t$ , conformal time,  $\eta$ , and our time variable  $x = \ln(a)$ . We also compute distance measures like the lumi-

nosity distance,  $d_L$ . Our fiducial cosmology is based on a fit of the 2018 Planck data parameter constraints by Aghanim et al. (2020). We will compare this model fit with an MCMC fit from supernova data by Betoule et al. (2014). The use of these two fit results along with the behaviour of our main parameters will be used to evaluate the validity of our background. Our model makes the assumptions that we can ignore the effects of neutrinos and polarization.

Once this is completed we move on to computing the Recombination era of our universe. In this time-frame we compute the tight coupling function  $\tau(x)$  and the visibility function  $\tilde{g}(x)$ . Among other results, we attempt to constrain a time where recombination is most likely to have occurred.

Moving on to the third phase of our investigation, we numerically compute a system of linearized Einstein-Boltzmann equation for the components of the universe; baryons ( $b$ ), cold dark matter (CDM), and photons ( $\gamma$ ). This is done in Fourier Space over three  $k$  modes. The computed system of equations are used to evolve the density perturbations of the components and their velocity. We also compute the evolution of the multipoles  $\Theta_\ell$  of the CMB temperature, and the gravitational potentials,  $\Phi$  and  $\Psi$ .

In the end we construct the angular power spectrum of the CMB and the matter power spectrum.

## 2. Key symbols and fiducial cosmology

The purpose of this section is to allow the reader a reference point for future clarifications. The physics involved in this investigation requires several different symbols and annotations. As to not strain the reader by forcing them to search for definitions throughout the four main sections of this paper, we have created a table for reference. Table 1 contains a list explaining some symbol definitions as well as some equations where you can find them. Only equations in which the variables are defined or a significant part of the equation will be mentioned. The purpose of this is to have an accessible reference point to the significance and definition of important symbols.

**Table 1.** Table containing the explanation of symbols used throughout this investigation and the equations in which they are used significantly or defined.

Symbol	Description	Equation
$t$	cosmic time	Eq. 7
$a$	scale factor	Eq. 7, 16
$H$	Hubble parameter	Eq. 7, 22
$g_{\mu\nu}$	FRWL metric	Eq. 45
$\eta$	conformal time	Eq. 8
$c$	speed of light	Eq. 8, 23
$\mathcal{H}$	Conformal Hubble parameter	Eq. 16, 8
$\chi$	comoving distance	Eq. 17
$d_A$	angular diameter distance	Eq. 19
$d_L$	luminosity distance	Eq. 20
$\tau$	optical depth	Eq. 24
$\sigma_T$	Thomson cross-section	24, 25
$\alpha$	the fine structure constant	
$\hbar$	reduced Planck constant	
$n_e$	electron number density	Eq. 24, 25
$n_H$	proton number density	Eq. 28, 29
$X_e$	free electron fraction	Eq. 28, 30, 31
$\tilde{g}$	visibility function	Eq. 26, 44
$\delta_i$	density perturbation of $i$	
$v_i$	velocity of $\delta_i$	
$\Psi$	gravitational potential	Eq. 58
$\Phi$	gravitational potential	Eq. 57

Our fiducial cosmology is based off of a fit to the Plank 2018 data, Aghanim et al. (2020). The parameters of this fit can be seen below. It is important to note that we ignore the effects of neutrinos and polarization unless stated otherwise.

$$\begin{aligned}
 h &= 0.67, \\
 T_{\text{CMB}} &= 2.7255 \text{ K}, \\
 N_{\text{eff}} &= 3.046, \\
 \Omega_{b0} &= 0.05, \\
 \Omega_{\text{CDM}0} &= 0.267, \\
 \Omega_{k0} &= 0, \\
 \Omega_{\nu0} &= N_{\text{eff}} \cdot \frac{7}{8} \left( \frac{4}{11} \right)^{4/3} \Omega_{\gamma0}, \\
 \Omega_{\Lambda0} &= 1 - (\Omega_{k0} + \Omega_{b0} + \Omega_{\text{CDM}0} + \Omega_{\gamma0} + \Omega_{\nu0}), \\
 n_s &= 0.965, \\
 A_s &= 2.1 \cdot 10^{-9}, \\
 Y_p &= 0.245, \\
 z_{\text{reion}} &= 8, \\
 \Delta z_{\text{reion}} &= 0.5, \\
 z_{\text{Hereion}} &= 3.5, \\
 \Delta z_{\text{Hereion}} &= 0.5.
 \end{aligned}$$

This cosmology follows the best-fit cosmology results from the 2018 Planck data, Aghanim et al. (2020).

## 3. Background Cosmology

Our final goal of this project is to compute the angular power spectrum of Cosmic Microwave Background (CMB), and the matter power spectrum. In order to do so, we must first lay the foundation for the background cosmology. In this section, we will compute the expansion history of the universe. This involves computing the evolution of various matter and radiation density parameters, as well as the evolution of the conformal Hubble parameter  $\mathcal{H}$ .

We have employed the fiducial cosmology as described in Section 2, and assume a flat expanding universe following the  $\Lambda\text{CDM}$  model. As a simplification we do not consider neutrinos in our background geometry. The purpose of this section is to set the foundation for the next parts of our project, and in doing so we evaluate our computations. We will be comparing our figures with those of Callin (2006) and Winther (2024b) throughout the project.

In this section, we have also attempted to constrain some of our cosmological parameters by utilizing a Markov Chain Monte Carlo (MCMC) method on supernova data from Betoule et al. (2014).

### 3.1. Theory

#### 3.1.1. Background geometry and measures of time

We assume a flat expanding universe that follows the  $\Lambda\text{CDM}$  model. The background geometry of our universe is described by the Friedmann-Robertson-Lemaître-Walker (FRLW) metric, Eq.(1)

$$ds^2 = -c^2 dt^2 + a^2(t)(dx^2 + dy^2 + dz^2) \quad (1)$$

$$= a^2(t)(-d\eta^2 + dx^2 + dy^2 + dz^2). \quad (2)$$

The metric is here given in Cartesian coordinates.

The FRLW metric can also be given in spherical coordinates,

$$ds^2 = -c^2 dt^2 + a^2(t) (dr^2 + r^2(d\theta^2 + \sin^2 \theta d\phi^2)) \quad (3)$$

$$= a^2(t)(-d\eta^2 + dr^2 + r^2(d\theta^2 + \sin^2 \theta d\phi^2)). \quad (4)$$

We have that  $c$  is the speed of light in a vacuum,  $a(t)$  is the scale factor,  $t$  is cosmic time and  $\eta$  is the conformal time. In the FRLW metric with Cartesian coordinates,  $x$ ,  $y$  and  $z$  are spatial coordinates. Note, this nomenclature can be disregarded for the rest of the project, as we will not be defining spatial coordinates in terms of  $x$ ,  $y$  or  $z$ .

Cosmic time,  $t$ , is the "normal" timescale most people are familiar with, typically given in SI units  $s$ . Our primary time variable will be what we define as  $x = \ln(a)$ . This for easier comprehension when dealing with such large timescales as what we will be dealing with.

The scale factor,  $a$ , is given by

$$a = \frac{1}{1+z} \quad (5)$$

$$a(x) = e^x \quad (6)$$

where  $z$  is the redshift and  $e^x$  is our scale factor for our time variable  $x = \ln(a)$ .

We define the cosmic time as

$$t(x) = \int_0^a \frac{da}{aH} = \int_{-\infty}^x \frac{dx'}{H(x')}, \quad (7)$$

where  $H$  is the Hubble parameter,  $x = \ln(a)$  and  $x'$  is used to distinguish a specific time value  $x$  which we integrate to and the variable we integrate over.

The conformal time is given by

$$\eta = \int_0^t \frac{cdt'}{a(t')} = \int_0^a \frac{cda}{a^2 H} = \int_{-\infty}^x \frac{cdx'}{\mathcal{H}(x')}, \quad (8)$$

where  $\mathcal{H}$  is the conformal Hubble parameter, Eq.(16). The value of  $\eta$  from  $t = 0$  to  $t = \text{today}$  gives us the total comoving distance light could have travelled since the beginning of time, (Dodelson (2020), p.34). Note that in order to get conformal time in units of time as we are used to, i.e. seconds or years, we must compute  $\eta/c$ . This is usually how we will be presenting conformal time in this project.

The Hubble parameter is given as,

$$H = \frac{1}{a} \frac{da}{dt} \quad (9)$$

$$= H_0 \sqrt{(\Omega_{b0} + \Omega_{CDM0})a^{-3} + (\Omega_{\gamma0} + \Omega_{\nu0})a^{-4} + \Omega_{k0}a^{-2} + \Omega_{\Lambda0}},$$

where  $t$  is cosmic time and  $H_0$  is the Hubble constant.

The parameter  $\Omega_{i0}$  is the density parameter of  $i$  today, where  $i$  can represent baryons ( $b$ ), Cold Dark Matter ( $CDM$ ), photon radiation ( $\gamma$ ), massless neutrinos ( $\nu$ ), and the curvature of the universe ( $k$ ). Since we ignore neutrinos, we will always set  $\Omega_{\nu0} = 0$ .

The density parameters as a function of the scale factor,  $a$ ,  $\Omega_i(a)$  can be written as

$$\Omega_k(a) = \frac{\Omega_{k0}}{a^2 H(a)^2 / H_0^2} \quad (10)$$

$$\Omega_{CDM}(a) = \frac{\Omega_{CDM0}}{a^3 H(a)^2 / H_0^2} \quad (11)$$

$$\Omega_b(a) = \frac{\Omega_{b0}}{a^3 H(a)^2 / H_0^2} \quad (12)$$

$$\Omega_\gamma(a) = \frac{\Omega_{\gamma0}}{a^4 H(a)^2 / H_0^2} \quad (13)$$

$$\Omega_\nu(a) = \frac{\Omega_{\nu0}}{a^4 H(a)^2 / H_0^2} \quad (14)$$

$$\Omega_\Lambda(a) = \frac{\Omega_{\Lambda0}}{H(a)^2 / H_0^2}. \quad (15)$$

With the exception of  $\Omega_k$ , the density parameters of the previously described constituents can be divided into the sub groups of radiation, matter and dark energy. Throughout this text, the density parameters will often be referred to as  $\Omega_i$  for radiation in general,  $\Omega_m = \Omega_b + \Omega_{CDM}$  for matter and  $\Omega_\Lambda$  for dark energy.

In most sections of this project we will be referring to the conformal Hubble,  $\mathcal{H}$ , parameter which is defined similarly to the non-conformal Hubble parameter  $H(t)$ . We have that

$$\mathcal{H} = \frac{1}{a} \frac{da}{d\eta} = aH, \quad (16)$$

where  $\eta$  is the conformal time from Eq.(8).

### 3.1.2. Distance measures

The comoving distance,  $\chi$ , is heavily related to the conformal time  $\eta$ . We define the comoving distance between  $x = 0$  to a time  $x$  as,

$$\chi = \int_0^x \frac{cdx'}{\mathcal{H}(x')} = \eta_0 - \eta(x), \quad (17)$$

where  $\eta_0$  is the conformal time today and here  $\eta(x)$  is the value of  $\eta$  at time  $x$ . The comoving distance between two points will remain constant with the expansion of the universe. It is a measure of the maximum distance unobstructed light can travel in the given time interval (ex.  $x \in [0, x]$ ).

The radial distance coordinate,  $r$ , of the spherical FRLW is dependent on the comoving distance and density parameter of the curvature of the universe today,  $\Omega_{k0}$ . We have that  $r$  is given by

$$r = \begin{cases} \chi \cdot \frac{\sin(\sqrt{|\Omega_{k0}|} H_0 \chi / c)}{(\sqrt{|\Omega_{k0}|} H_0 \chi / c)} & \Omega_{k0} < 0 \\ \chi & \Omega_{k0} = 0 \\ \chi \cdot \frac{\sinh(\sqrt{|\Omega_{k0}|} H_0 \chi / c)}{(\sqrt{|\Omega_{k0}|} H_0 \chi / c)} & \Omega_{k0} > 0. \end{cases} \quad (18)$$

The three different cases of  $r$  are for:  $\Omega_{k0} < 0$  a closed universe,  $\Omega_{k0} = 0$  a flat universe, and  $\Omega_{k0} > 0$  an open universe.

Once we know the radial distance  $r$ , we may use it to find the angular diameter distance  $d_A$  and the luminosity distance  $d_L$ .

The angular diameter distance  $d_A$  is given by

$$d_A = ar, \quad (19)$$

where  $a$  is the scale factor as a function of cosmic time and  $e^x$  is the scale factor in our time variable  $x = \ln(a)$ .

The luminosity distance is related to the angular diameter distance and is defined as

$$d_L = \frac{r}{a} = \frac{d_A}{a^2}. \quad (20)$$

### 3.1.3. Statistics

The  $\chi^2$  function is utilized when we want to check the likelihood of all the possible values of our parameters. It is given by

$$\chi^2(h, \Omega_{m0}, \Omega_{k0}) = \sum_{i=1}^N \frac{[(d_L(z_i, h, \Omega_{m0}, \Omega_{k0}) - d_L^{obs}(z_i))^2]}{\sigma_i^2}, \quad (21)$$

where  $d_L^{obs}$  is the observed distance luminosity,  $N$  is the number of data points from our observations and  $\sigma_i$  is the standard estimated error of data point  $i$ .

A low  $\chi^2$  means that the choice of the parameters have a high likelihood. A fit is considered good if  $\frac{\chi^2}{N} \sim 1$ .

### 3.2. Implementation details

We implemented the fiducial parameters given by Aghanim et al. (2020) in a class which computes our results. Our time  $x$  is set up as an array from  $x \in [-18, 5]$ , during plotting our x-array contained the number of points,  $n = 4 \cdot 10^5$  during plotting for an increased resolution. However, when we moved on from the background geometry we set  $n = 10^4$ , as this was sufficient for our calculations. The x-array was splined with result arrays, so that we could observe the results over time.

We computed the cosmic time  $t$ , and the conformal time  $\eta$  by integrating their derivatives as ODEs using a built-in RungeKutta4 ODE solver.

The cosmic time,  $dt$ , ODE is given as

$$\frac{dt}{dx} = \frac{1}{H}. \quad (22)$$

The conformal time,  $d\eta$ , ODE is given as

$$\frac{d\eta}{dx} = \frac{c}{\mathcal{H}}. \quad (23)$$

We then computed our results, using the physics defined in Sec. 3.1. Note that although we assume a flat universe in this project, we implemented the function for  $r$  for all three cases shown in Eq.(18). This is necessary for when we will need to find the best fit value of  $\Omega_{k0}$ , when attempting to constrain our cosmological parameters to fit to the supernova data from Betoule et al. (2014).

When using the supernova data from Betoule et al. (2014) to constrain our cosmological parameters, we employed a built-in Markov Chain Monte Carlo (MCMC) method on our computed background for  $10^4$  iterations. The MCMC method attempts to find the smallest  $\chi^2$ , see Eq.(21), for the parameters  $\Omega_{m0}$ ,  $\Omega_{k0}$ , and  $h$ . We recorded the output for each iteration and used the iteration with the smalles  $\chi^2$ . We then plotted the  $d_L$  using our best fit with the supernova data and the original fiducial cosmology, see Fig.(10).

The when plotting the posterior probability distribution functions (PDF) we assumed a Gaussian distribution. Additionally, we only plotted the  $1\sigma$  values of the given parameter. Meaning we plotted the distribution of only the most likely parameters, of which our best fit parameter value is in.

#### 3.2.1. Milestone times

There are three milestones of the background evolution that we are interested in; the radiation-matter (RM) equality time, matter-dark energy equality (MA) time and the time for which the expansion of our universe starts to accelerate,  $\frac{d^2a}{dt^2} > 0$ .

Calculating the RM equality point is simply done by finding the  $x$  time for which  $\Omega_b + \Omega_{CDM} = \Omega_\gamma + \Omega_\nu$ . Similarly for the MA equality we find the  $x$  time for which  $\Omega_b + \Omega_{CDM} = \Omega_\Lambda$ . Once we have the time in  $x$ , we convert them to  $z$  and  $t$  using Eq.(5) and Eq.(7) respectively.

When it comes to the acceleration time, it is sufficient to find the time when  $\frac{d^2a}{dt^2} = 0$ , as after this the expansion of the universe will accelerate.

We derive this time from setting inserting Eq.(9) into Eq.(16) and deriving with respect to cosmic time  $t$ . This gives us:

$$\begin{aligned} \mathcal{H} &= aH = \frac{a}{a} \frac{da}{dt} \\ \Rightarrow \frac{d\mathcal{H}}{dt} &= \frac{d^2a}{dt^2}. \end{aligned}$$

From here we insert the relation  $dt = \frac{dx}{H}$ , from Eq.(22) on the left side and get that:

$$\frac{d\mathcal{H}}{dx} H = \frac{d^2a}{dt^2}.$$

Both  $\frac{d\mathcal{H}}{dx}$  and  $H(x)$  have been computed when computing our background. Due to splining these results for our x-array, we easily retrieved the information for when  $\frac{d^2a}{dt^2} = 0$ .

### 3.3. Results

#### 3.3.1. Fiducial cosmology validation and evolution

For many of our figures, we have considered the evolution of our background cosmology in three regions, each which have their own color: radiation dominated (yellow), matter dominated (blue) and dark energy dominated (magenta).

In Fig.(5) we have plotted evolution of the radiation density parameter  $\Omega_\gamma$ , the matter density parameter  $\Omega_M$  and the dark energy density parameter  $\Omega_\Lambda$ . Additionally the sum of all three are plotted. Our first validation check point is to make sure that this sum always maintains at 1, which can clearly be seen in the figure.

The radiation-matter equality and the matter-dark energy equality times can be found in Table(2). The table also includes the age of the universe from  $x = -18.0$  to  $x = 0$  today in cosmic time and in conformal time, and the time for when the universe expansion started accelerating.

**Table 2.** Milestones in the cosmology of our computed universe given in our time variable  $x$ , redshift  $z$  and cosmic time  $t$ . The age of the universe given is from our simulation.

	x	z	t
RM-equality	-8.658	5754	23200 yrs
MA-equality	-0.2559	0.2916	10.38 Gyrs
Acc. started	-0.4867	0.6270	7.756 Gyrs
Age of universe	0	0	13.86 Gyrs
Age in conformal time	0	0	46.52 Gyrs

Our second validation check point arrives in the analysis of  $\mathcal{H}$  and its derivatives. During the radiation dominated era the conformal Hubble parameter  $\mathcal{H}$  is expected to fall to the order of  $\frac{1}{x}$ , which is  $e^{-x}$ . The reason for this can be seen in Eq.(9) where if we set the other density parameters to zero and  $\Omega_\gamma = 1$ ,  $\mathcal{H}$

which is  $aH$  should decrease to the order of  $a^{-1}$ . The expected behaviour is indicated with a blue dotted line in Fig.(1). From Fig.(1) we can interpret the behaviour that the expansion of the universe at  $x = -18$  decelerates and over time slows down until about  $x = -0.4867$  (see Table(2)) when the acceleration is zero. After this the behaviour of the  $\mathbf{H}$  indicates that the expansion of the universe will continue to accelerate.

### Conformal Hubble parameter $\mathcal{H}(x)$

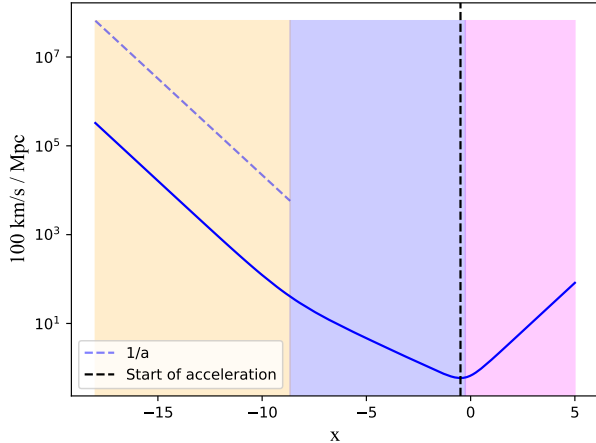


**Fig. 1.** Conformal Hubble parameter plotter as a function of time  $x$ . The dotted black line indicates the time the expansion of the universe started accelerating,  $\frac{d^2a}{dt^2} = 0$ . The dotted blue line indicates the analytically predicted behaviour of  $\mathcal{H}$  during the radiation dominated region. The yellow region indicates the radiation dominated era, the blue region indicates the matter dominated era, and the magenta region indicates the dark energy dominated era.

Moving on to Fig.(2), where we have plotted the derivatives of  $\mathcal{H}$  divided by  $\mathcal{H}$ . The dotted lines, which are color coded to their era indicate the analytically calculated value of the derivatives of  $\mathcal{H}$  for when each of the density parameters are 1 and the rest are 0. Our analytical expectations are clearly met in the figure, which is the third validation of our model. The expected analytical values for each regime are the following.

$$\Omega_\gamma = 1$$

$$\begin{aligned} \frac{d\mathcal{H}(x)}{dx} \frac{1}{\mathcal{H}(x)} &= -1 \\ \frac{d^2\mathcal{H}(x)}{dx^2} \frac{1}{\mathcal{H}(x)} &= 1 \end{aligned}$$

$$\Omega_M = 1$$

$$\begin{aligned} \frac{d\mathcal{H}(x)}{dx} \frac{1}{\mathcal{H}(x)} &= -\frac{1}{2} \\ \frac{d^2\mathcal{H}(x)}{dx^2} \frac{1}{\mathcal{H}(x)} &= \frac{1}{4} \end{aligned}$$

$$\Omega_\Lambda = 1$$

$$\begin{aligned} \frac{d\mathcal{H}(x)}{dx} \frac{1}{\mathcal{H}(x)} &= 1 \\ \frac{d^2\mathcal{H}(x)}{dx^2} \frac{1}{\mathcal{H}(x)} &= 1 \end{aligned}$$

Our last validation check is in Fig.(3), where we have plotted the behaviour of the conformal time  $\eta(x)$ , and its derivatives,

### Validation plot of the $\mathcal{H}(x)$ derivatives' behavior

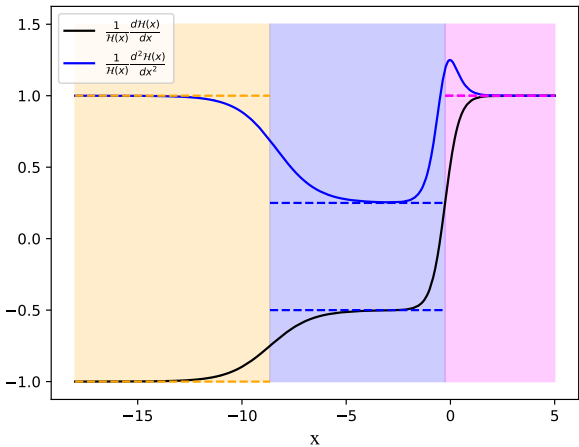


**Fig. 2.** Plot of the derivatives of  $\mathcal{H}(x)$ 's behavior. The yellow region indicates the radiation dominated era, the blue region indicates the matter dominated era, and the magenta region indicates the dark energy dominated era. The dotted lines are analytical solutions to the product of the first or second order derivative of  $\mathcal{H}(x)$  divided by  $\mathcal{H}(x)$  for when the density parameters of  $\Omega_i$  are 1. The analytical values are color coded according to domination regime.

multiplied by  $\frac{\mathcal{H}}{c}$ . Analytically, we know that in early times, f.ex.  $x = -18$ ,  $\eta \approx \frac{c}{\mathcal{H}}$ . Thus, for early times we should get that  $\frac{\eta\mathcal{H}}{c} = 1$ , which can easily be seen in Fig.(3). From Eq.(23), we know that the derivative of  $\eta$  is equal to  $\frac{c}{\mathcal{H}}$ . Therefore, we know that  $\frac{d\eta}{dx} \frac{\mathcal{H}}{c} = 1$  always. Which is also validated by Fig.(3).

### Validation plot of $\eta(x)$ behavior

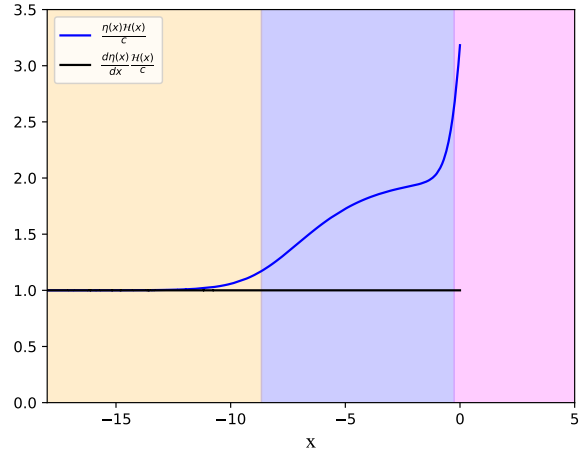


**Fig. 3.** Behavior of  $\frac{\eta\mathcal{H}}{c}$  and  $\frac{d\eta}{dx} \frac{\mathcal{H}}{c}$ . The yellow region indicates the radiation dominated era, the blue region indicates the matter dominated era, and the magenta region indicates the dark energy dominated era.

In Fig.(4) we have plotted the conformal time  $\eta/c$  and the cosmic time  $t$  as functions of our time variable  $x$ . The dotted gray line indicates the current age of our universe in cosmic time  $t$ . As previously established, the conformal time,  $\eta(x)$ , tells us how far an unobstructed photon can travel from time  $x = 0$  to  $x = x$ . The conformal time,  $\eta(x)/c$ , gives us the time it would take for an unobstructed photon to travel that length. In other words,  $\eta(x)/c$  is the longest amount time a photon can have spent traveling with-

out obstructions from the beginning of time until a time  $x$ . In Fig.(4), we see that the timescales of both conformal and cosmic time are increasing with  $x$  until we reach the dark energy dominated era. In the  $\Lambda CDM$  model dark energy is thought to be responsible for the acceleration of the expansion of the universe. In this region in Fig.(4) we see that the growth of the conformal time slows down, indicating that the universe is expanding at an increased speed. The growth of conformal time slows down as a consequence of the scale factor  $a(t)$  increasing. This is due to the relation  $\frac{d\eta/c}{dx} = \frac{dt}{a(t)}$ .

### Cosmic time and conformal time in relation to $x$

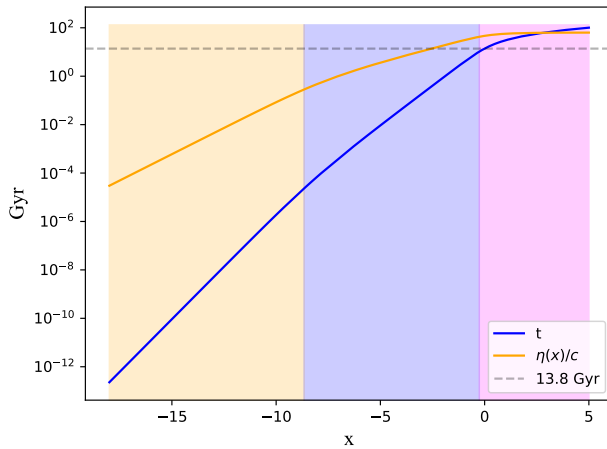


**Fig. 4.** Plot of the conformal time  $\eta(x)/c$  and the cosmic time  $t$  as functions of  $x$ . The dotted gray line indicates the age of our universe in cosmic time  $t$  today. The yellow region indicates the radiation dominated era, the blue region indicates the matter dominated era, and the magenta region indicates the dark energy dominated era.

### Evolution of $\Omega_{i0}$

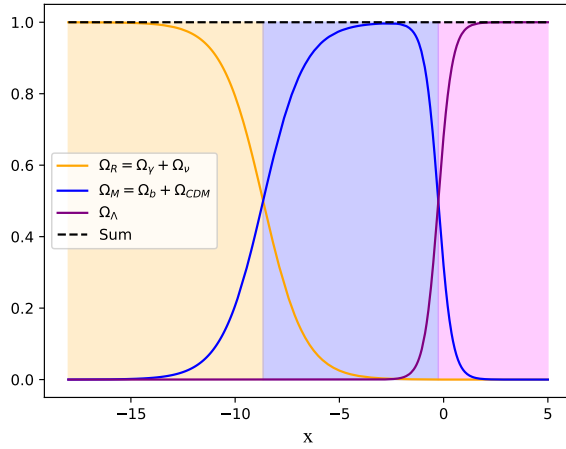


**Fig. 5.** Plot of the evolution of each of the density parameters  $\Omega_i$ .  $\Omega_M$  is the sum of the density parameter for baryons,  $\Omega_b$ , and CDM,  $\Omega_{CDM}$ .  $\Omega_R$  is the sum of the density parameters for the radiation terms  $\Omega_\gamma$  and  $\Omega_\nu = 0$ .  $\Omega_\Lambda$  is the density parameter for dark energy. The yellow region indicates the radiation dominated era, the blue region indicates the matter dominated era, and the magenta region indicates the dark energy dominated era.

### 3.3.2. MCMC results

**Table 3.** Values of the parameters constrained using MCMC method and their standard deviation compared to parameters and their errors in Betoule et al. (2014) and the Planck 2018 results of Aghanim et al. (2020).

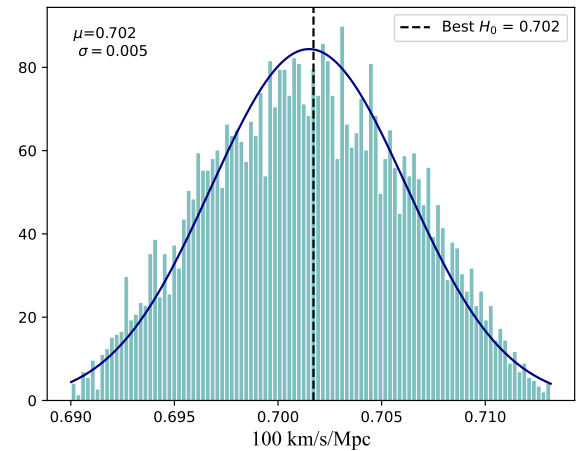
Min. $\chi^2 = 29.28$	Parameter value	STD of parameter
$\Omega_{m0}$	0.255	$\pm 0.084$
$\Omega_{k0}$	0.0790	$\pm 0.210$
$H_0$ [km / s / Mpc]	70.17	$\pm 0.5$
<b>Betoule 2014</b>	<b>Parameter value</b>	<b>Uncertainty</b>
$\Omega_{m0}$	0.295	$\pm 0.034$
<b>Planck 2018</b>	<b>Parameter value</b>	<b>Uncertainty</b>
$\Omega_{m0}$	0.315	$\pm 0.007$
$\Omega_{k0}$	0.001	$\pm 0.002$
$H_0$ [km / s / Mpc]	67.4	$\pm 0.5$

Our best fit was made using the minimum  $\chi^2$  value, which we found to be 29.28. All the figures that show our best fit results and parameter constraints are from the  $1\sigma$  (68.4%) confidence region of our MCMC fit, with the exception of Fig.(9). As shown in Table(3) our best fit parameters are  $\Omega_{k0} = 0.0790$ ,  $\Omega_{m0} = 0.255$ , and  $H_0 = 70.17$ . The posterior probability distributions (PDF) of the individual parameters can be seen in Figs.(7, 8, 6), respectively. We note that all the parameter's best fit values are within the standard deviation of their individual PDFs, showing that our best fit is comprised of parameters with a high likelihood. More objectively, the goodness of our fit can be judged by  $\chi^2/N$  where  $N$  is the number of data points. We found our goodness of fit to be

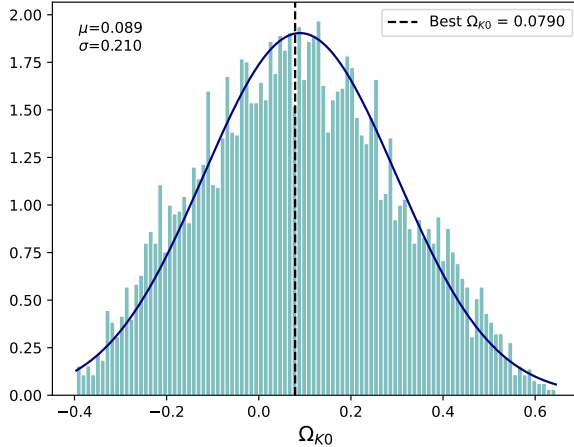
$$\frac{\chi^2}{N} = \frac{29.28}{31} = 0.9445,$$

which is close to 1, indicating that we have not over or under fitted.

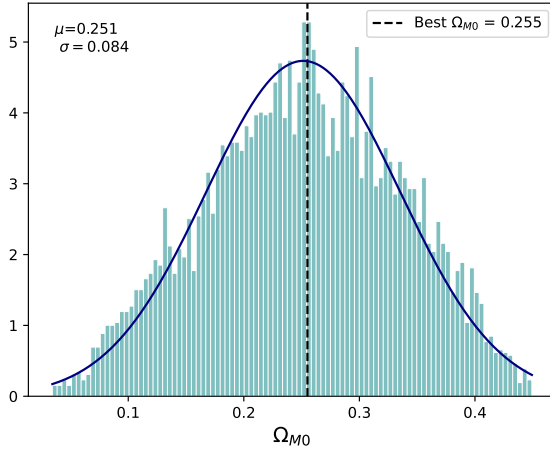
### Posterior PDF of $H_0$



**Fig. 6.** Posterior probability distribution function of  $H_0$  in the  $1\sigma$  confidence region of MCMC best fit.

**Posterior PDF of  $\Omega_{k0}$** 

**Fig. 7.** Posterior probability distribution function of  $\Omega_{k0}$  in the  $1\sigma$  confidence region of MCMC best fit.

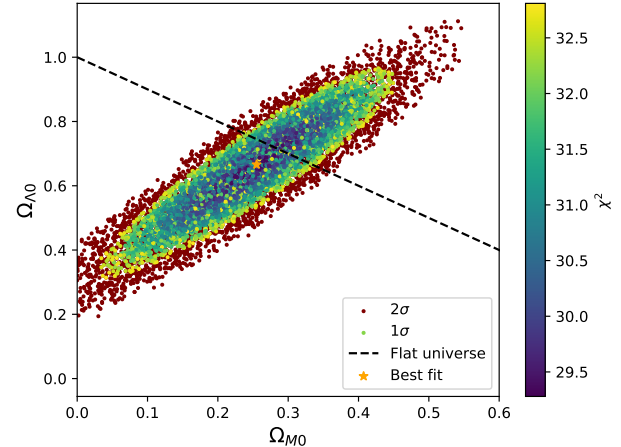
**Posterior PDF of  $\Omega_{m0}$** 

**Fig. 8.** Posterior probability distribution function of  $\Omega_{m0}$  in the  $1\sigma$  confidence region of MCMC best fit.

In Fig.(9) we have plotted the  $1\sigma$  and  $2\sigma$  confidence region for the  $\Omega_{m0}$  and  $\Omega_{\Lambda 0}$  cosmological parameters, with our best fit values of the two marked as an orange star. The dotted line indicates the parameter values of  $\Omega_{m0}$  and  $\Omega_{\Lambda 0}$  which satisfy a flat universe with  $\Omega_{k0} = 0$ .

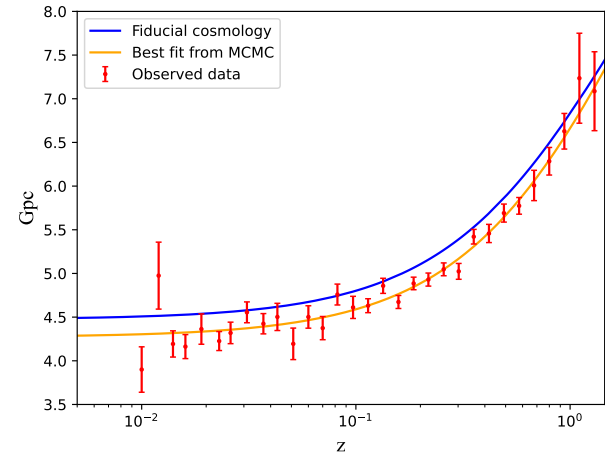
Judging Fig.(9) by eye it is clear that our best fit model aligns with the flat universe model, although, not perfectly. In Table(3) we see that our best fit  $\Omega_{k0}$  is 0.0790 with a standard deviation of  $\pm 0.210$ , which is close to flat, but not as close as the Planck 2018 constraints. When looking further, we also see that our  $\Omega_{k0}$  parameter's standard deviation is close to 100 times larger than the estimated error of the Planck 2018 results. This makes our best fit model look quite rough in comparison. However, that is to be expected when considering the simplifications we have made in our background cosmology and the fact that we only have 31 data points from Betoule et al. (2014) to fit to.

In Fig.(10) we have compared the luminosity distance  $d_L$  found using the constrained parameters from the MCMC fit of the data from Betoule et al. (2014), to that of the fiducial cos-

**Confidence region of  $\Omega_{m0}$  vs  $\Omega_{\Lambda 0}$** 

**Fig. 9.**  $1\sigma$  and  $2\sigma$  confidence region for the  $\Omega_{m0}$  and  $\Omega_{\Lambda 0}$ . Best fit is marked with an orange star. The dotted line indicates the parameter values of  $\Omega_{m0}$  and  $\Omega_{\Lambda 0}$  for a  $\Omega_{k0} = 0$ .

mology we gathered from a fit of the Planck 2018 data. Despite a clear difference in the two fits, we see that the luminosity distances become more similar with higher redshifts  $z$ . It is clear that our fiducial cosmology fit does not align perfectly with the observed data from Betoule et al. (2014). In Table(3), only one parameter constraint with a given error is given from the Betoule et al. (2014) paper, that of  $\Omega_{m0}$ . The paper constrained  $\Omega_{m0}$  to a value of  $0.295 \pm 0.034$ , which is an uncertainty closer to five times larger than the Planck 2018 results. Given the precision of the Planck 2018 data, our analysis favours the original fiducial cosmology over that of the MCMC fit of the Betoule et al. (2014) data.

 **$d_L/z$  of best fit and supernova data**

**Fig. 10.** Plot of the luminosity distance,  $d_L$ , using the best fit parameters from the MCMC method in orange and the fiducial cosmology in blue. The observed data is plotted as red dots with their respective error-bars. The MCMC fit has a goodness of fit value of  $\chi^2/N = 0.9445$ , indicating that we have a good fit. The  $d_L$  and errorbars are normalized with respect to the redshift  $z$  for easier comparison.

## 4. Recombination

As we have previously set the scene by modeling the background cosmology of our universe, it is now time to move on. For this section of our investigation, our goal is to model the recombination history of our universe.

The epoch of Recombination defines a time in the evolution of the universe when electrons and protons combined to form neutral hydrogen, a process which was triggered by the expansion and cooling of the universe.

At very early times, the photon-baryon fluid, which the universe consisted of, was hot and tightly coupled, causing the fluid to be an optically dense medium in which photons could not freely move. The expansion and cooling of the universe allowed the photons to become less energetic and in turn less optically dense. Eventually, the expansion and cooling allowed for the formation of hydrogen which could combine with free electrons.

This period in the history of the universe allowed space to go from an optically dense medium filled with free electrons, which scattered photons, to an optically thin medium where photons can travel for several million light years and reach the Earth. This epoch of the universe is therefore a pivotal point in history which has allowed us to study the evolution of the universe through observations today.

This stage of our investigation will detail the theory behind recombination which we use to set up our model of the CMB power spectrum. We will attempt to determine the optical depth,  $\tau(x)$ , as a function of our variable  $x$ , where  $x = \ln(a)$ , of the medium of space in the time before recombination up until today. Through  $\tau(x)$  we will determine the visibility function  $\tilde{g}(x)$ . Finally, we will find the time of the last scattering surface expressed in our time variable  $x$ , the redshift  $z$  and in cosmic time  $t$ , and in the end determine the sound horizon at decoupling in our model, which will be of help in the next stage of our investigation.

### 4.1. Theory

Before recombination, all atoms were fully ionized, causing the universe to consist of a tightly coupled plasma of baryons and photons. This plasma inhibited the free movement of photons, making space an optically dense medium (Section 4.1.1), through the effect of Thomson scattering which describes the scattering of radiation by free electrons, Crowley & Gregori (2014).

It is worth noting that although Thomson scattering is not the only form of scattering present during the time before recombination, it is the main contributor to an increase in optical depth,  $\tau$ .

The main culprit of all photon scattering is the free electrons in the plasma, as the photons scattered off of protons are negligible due to their mass being much larger than the mass of an electron. The mass of the baryon is of significance as the scattering cross section,  $\sigma$ , which is proportional to the rate of which the photon-particle interaction will occur Kotlarchyk (1999), is also proportional to  $\frac{1}{m^2}$  where  $m$  is the mass of the particle. Due to this, the decoupling of photons from baryons can be indicated from the free electron fraction,  $X_e$ , itself. According to Dodelson (2020), the decoupling is thought to occur by  $X_e \approx 10^{-2}$ .

With this in mind, we can determine the time of the photon decoupling and the time of recombination from the interpretation of  $\tau(x)$ ,  $\tilde{g}(x)$ , and  $X_e(x)$ .

This section will give an introduction to the theoretical descriptions of the physics necessary to understand recombination, and what we can find out from the results of our model.

#### 4.1.1. The optical depth and the visibility function

The optical depth,  $\tau$ , determines the visibility of a medium and is given by

$$\tau(\eta) = \int_{\eta}^{\eta_0} c n_e \sigma_T d\eta', \quad (24)$$

where  $\eta$  is the conformal time,  $n_e$  is the number density of electrons and  $\sigma_T$  is the Thomson cross-section,  $\sigma_T = \frac{8\pi}{3} \frac{e^2 h^2}{m_e^2 c^2}$ . See Tab 1 for further explanation of symbols. When  $\tau \ll 1$  the medium is considered optically thin and photons can easily pass through the medium. When  $\tau \gg 1$  the medium is considered optically thick, and photons are unable to pass through.

The differential form of  $\tau$  with respect to our time parameter  $x$  can be written as

$$\frac{d\tau}{dx} = -\frac{c n_e \sigma_T}{H}, \quad (25)$$

where  $H$  is the Hubble parameter.

From the  $\tau(x)$  and its derivative we can determine the visibility function

$$\tilde{g}(x) = -\tau' e^{-\tau}. \quad (26)$$

The visibility function is a probability distribution that determines the probability distribution of a photon having last scattered at a time  $x$ .

#### 4.1.2. $X_e$ and model assumptions

The free electron fraction,  $X_e$ , is a measure of the electron to nucleon ratio given by

$$X_e = n_e / n_b, \quad (27)$$

where  $n_b$  is the number density of baryons. In our model, we assume that all baryons are protons and ignore the heavier elements like helium. Therefore  $X_e$  becomes

$$X_e = n_e / n_H, \quad (28)$$

where  $n_H$  is the number density of protons.

We also ignore the small mass differences between free protons and neutral hydrogen, so that we have

$$n_H = n_b \approx \frac{\rho_b}{m_H} = \frac{\Omega_{b0} \rho_{c0}}{m_H a^3}, \quad (29)$$

where  $\rho_{c0} \equiv \frac{3H_0^2}{8\pi G}$ .

#### 4.1.3. The Saha approximation and the Peebles equation

We will be using two equations to find  $X_e$ . The first one is the Saha approximation.

The Saha approximation is given by

$$\frac{X_e^2}{(1 - X_e)} = \frac{1}{n_b} \left( \frac{k_b T m_e}{2\pi \hbar^2} \right)^{3/2} \exp\left(-\frac{\epsilon_0}{k_b T_b}\right), \quad (30)$$

where  $k_b$  is the Boltzmann constant,  $T_b$  is the baryon temperature, and  $\epsilon_0$  is the binding energy of hydrogen at 13.6 eV. The Saha approximation is valid before recombination.

After recombination, we must use the Peebles equation. This equation is given by

$$\frac{dX_e}{dx} = \frac{C_r(T_b)}{H} \left[ \beta(T_b)(1 - X_e) - n_H \alpha^{(2)}(T_b) X_e^2 \right]. \quad (31)$$

The variables used in the Peebles equation are described in the following set of equations

$$C_r(T_b) = \frac{\Lambda_{2s \rightarrow 1s} + \Lambda_\alpha}{\Lambda_{2s \rightarrow 1s} + \Lambda_\alpha + \beta^{(2)}(T_b)}, \quad (\text{dimensionless}) \quad (32)$$

$$\Lambda_{2s \rightarrow 1s} = 8.227 s^{-1}, \quad (33)$$

$$\Lambda_\alpha = H \frac{(3\epsilon_0)^3}{(8\pi)^2 c^3 \hbar^3 n_{1s}}, \quad (\text{dimension 1/s}) \quad (34)$$

$$n_{1s} = (1 - X_e) n_H, \quad (\text{dimension 1/m}^3) \quad (35)$$

$$n_H = (1 - Y_p) n_b, \quad (\text{dimension 1/m}^3) \quad (36)$$

$$n_b = (1 - Y_p) \frac{3H_0^2 \Omega_{b0}}{8\pi G m_H a^3}, \quad (\text{dimension 1/m}^3) \quad (37)$$

$$\beta^{(2)}(T_b) = \beta(T_b) e^{\frac{3\epsilon_0}{4k_b T_b}}, \quad (\text{dimension 1/s}) \quad (38)$$

$$\beta(T_b) = \alpha^{(2)}(T_b) \left( \frac{m_e k_b T_b}{2\pi \hbar^2} \right)^{3/2} e^{-\frac{\epsilon_0}{k_b T_b}}, \quad (\text{dimension 1/s}) \quad (39)$$

$$\alpha^{(2)}(T_b) = \frac{8}{\sqrt{3\pi}} c \sigma_T \sqrt{\frac{\epsilon_0}{k_b T_b}} \phi_2(T_b), \quad (\text{dimension m}^3/\text{s}) \quad (40)$$

$$\phi_2(T_b) = 0.448 \ln \left( \frac{\epsilon_0}{k_b T_b} \right), \quad (\text{dimensionless}). \quad (41)$$

#### 4.1.4. The sound horizon

The sound horizon is a cosmological scale that represents the maximum distance acoustic waves could travel in the early universe's photon-baryon plasma before the epoch of recombination. The sound horizon is given by

$$s(x) = \int_0^a \frac{c_s dt}{a} = \int_{-\infty}^x \frac{c_s dx}{\mathcal{H}} \rightarrow \frac{ds(x)}{dx} = \frac{c_s}{\mathcal{H}} \quad (42)$$

with  $s(x_{\text{ini}}) = \frac{c_s(x_{\text{ini}})}{\mathcal{H}(x_{\text{ini}})}$ , where  $c_s = c \sqrt{\frac{R}{3(1+R)}}$  is the speed of sound in the plasma, with  $R = \frac{4\Omega_{\gamma0}}{3\Omega_{b0}a}$  representing the ratio of photon to baryon density.

The sound horizon at recombination provides a measure for cosmological distances, enabling the determination of the universe's geometric properties from the acoustic peaks in the cosmic microwave background (CMB) and baryon acoustic oscillations (BAO), Arendse et al. (2019)

#### 4.2. Implementation details

Using the same fiducial cosmology from when we developed the background cosmology, we compute  $X_e$  and use the relation between  $X_e$  and  $n_e$  in Eq.(28) to solve for the  $n_e$  at the same time we solve for  $X_e$ . The time range in  $x$  for our model has been set to  $x \in [-18, 0]$  where  $x = 0$  represents our time today.

In our numerical model, we have implemented Runge-Kutta 4 ODE solvers to integrate, and created cubic splines of the solutions and the time  $x$ .

#### 4.2.1. Computing $X_e$

We first compute  $X_e$  using the Saha equation as the electron fraction  $X_e \approx 1$  in the early universe. In order to do so, we simply solve the Saha equation as a quadratic equation for  $X_e$ .

We set

$$\frac{1}{n_b} \left( \frac{k_b T_m e}{2\pi \hbar^2} \right)^{3/2} \exp\left(-\frac{\epsilon_0}{k_b T_b}\right) = C.$$

So that the Saha equation becomes

$$\frac{X_e^2}{(1 - X_e)} = C \rightarrow X_e^2 + CX_e - C = 0.$$

Solving this using the quadratic method gives

$$X_e = -\frac{C}{2} + \frac{C}{2} \sqrt{1 + \frac{4}{C}}.$$

In the early times  $C$  is quite large, so we make the approximation of  $\sqrt{1+x} \approx 1+\frac{x}{2}$  where  $x = 4/C$ . Employing this approximation gives us a second solution for  $X_e$  in the Saha regime. The second solution for large  $C$  is given simply as

$$X_e = -\frac{C}{2} + \frac{2}{C} = 1.$$

When the computation of the electron fraction decreases to a value of  $X_e < 0.9$ , we switch to solving the Ordinary Differential Equation (ODE) of the Peebles equation, 31 to compute  $X_e$ . We set the initial condition of the ODE as the last  $X_e$  value computed. Then we solve the ODE repeatedly for one time point at a time.

While we find  $X_e$  for our time range, we also find  $n_e$  by  $n_e = X_e \cdot n_H$ . We spline our results with our  $x$  range so that we may easily find the values for their respective  $x$  time point.

#### 4.2.2. Computing $\tau(x)$ and $\tilde{g}(x)$

Once we have found  $n_e$  we may numerically solve the ODE

$$\frac{d\tau}{dx} = -\frac{cn_e \sigma_T}{H}, \quad (43)$$

and find  $\tau(x)$ . We solve the ODE by computing it from  $x = 0$  to  $x = -18$  so that we can set the initial condition  $\tau(x = 0) = 0$ . From there we can calculate  $\tilde{g}(x)$  using Eq.(26). We analytically find the derivative of  $\tilde{g}(x)$  to be

$$\frac{d\tilde{g}(x)}{dx} = \exp(-\tau) ((\tau'^2 - \tau''). \quad (44)$$

After this, we use a built-in function to find  $\frac{d^2\tilde{g}(x)}{dx^2}$ .

#### 4.2.3. Methodology of analysis and computing the sound horizon

In order to find the times of the last scattering, recombination and the recombination in the Saha solution we use the following relations

$$x = \ln(a) \quad \text{and} \quad z = \frac{1}{\exp(x)} - 1.$$

We also use the function for the cosmic time, as described in Section 3. The time of the beginning of recombination we set to take place when  $X_e < 0.1$ . For the last scattering we find the  $x$  for when  $\tilde{g}(x)$  peaks, as this is when most photons are likely to have decoupled.

### 4.3. Results

#### 4.3.1. The free electron fraction $X_e$

The evolution of the free electron fraction  $X_e$  was determined using both the Saha approximation and the Peebles equation as functions of  $x$ . As shown in Figure 11,  $X_e$  starts close to unity, indicating a fully ionized universe, and decreases significantly as recombination progresses. Once  $X_e$  falls below 0.99 we switch to the Peebles approximation in our model. The figure is similar to that of Callin (2006), which we use to validate our model's accuracy.

The orange dashed line indicates how the evolution of  $X_e$  would occur according to the Saha approximation. It is well established that the Saha approximation is only accurate for  $X_e \approx 1$ , this concurs with our results where we see that the Saha approximation predicts recombination to have been completed  $x \approx -7.14$ , with an eventual electron fraction,  $X_e$ , of 0 at  $x \approx 6.9$ . In comparison, our combined model predicts a longer period of time in which recombination occurs. Our model predicts a recombination time of  $x = -6.988$ , seen in Table.(4), with  $X_e$  approaching a value of about  $1.985 \cdot 10^{-4}$ , for  $x = 0$ . Unlike the Saha prediction, the electron fraction,  $X_e$ , in our model never reaches zero. This is because the Saha approximation does not consider the *freeze out*, which is when the rate of expansion of the universe surpasses the rate of recombination.

It is worth mentioning that recombination did not all happen at once, but was rather a period of time in which electrons and protons combined to form neutral hydrogen. The time we estimate is the time when recombination is likely to have been completed.

Our model predicts that recombination occurs around the same time as we observe the last scattering, as predicted by  $\tilde{g}(x)$ , see Table4 and Fig. 11. This follows established literature, Dodelson (2020) p.72, where Dodelson states that recombination is directly tied to the decoupling of photons.

#### The electron fraction $X_e$ as a function of $x$

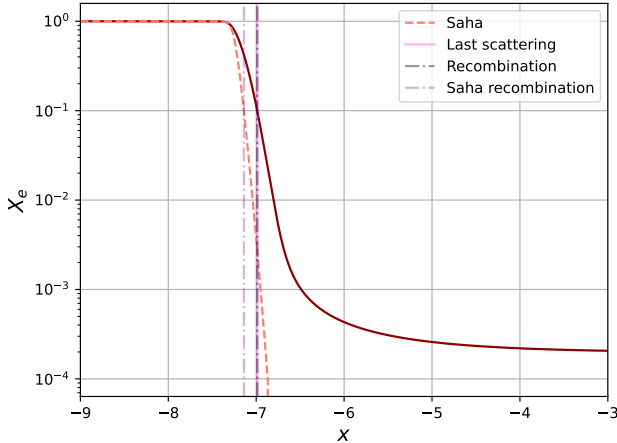


**Fig. 11.** The electron fraction  $X_e$  as a function of  $x$ , where  $x = \ln(a)$ . The orange dashed line is the evolution of  $X_e$  according to the Saha approximation. The solid dark line is our model evolution of  $X_e$ . We assume recombination to have begun by  $X_e < 0.1$ . The point where  $X_e = 0.1$  is marked by the grey dashed line. The pink solid line underneath is the time of the last scattering as predicted by the visibility function,  $\tilde{g}(x)$ .

### The optical depth $\tau(x)$ and its derivatives

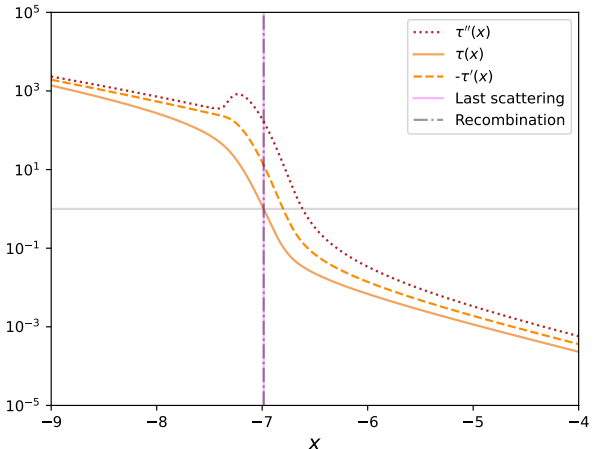


**Fig. 12.** The optical depth  $\tau$  and its derivatives as a function of  $x$  where  $x = \ln(a)$ . The solid horizontal gray line is the point where  $\tau = 1$ . This line coincides with the lines marking the time of the last scattering and the beginning of recombination.

#### 4.3.2. Decoupling and recombination times

The time when most photons have decoupled was found as described in 4.2.3, it is recorded in Table4 in  $x$ , redshift  $z$ , and cosmic time  $t$ . The table also contains the time when recombination is likely to have started, we have defined this as when  $X_e < 0.1$ , for our model using Peebles and Saha, as well as the predicted time for only the Saha approximation. The Saha recombination time was not used further in our model but is provided as a demonstration of the model's inaccuracy when  $X_e$  deviates from around 1.

The sound horizon at decoupling was calculated to be about 163.81 Mpc. We further discuss the meaning of this result in the next section.

**Table 4.** Table times of decoupling and the recombination time predicted by Saha and the model using Peebles as well.

	$x$	$z$	$t$ [Myr]
Photon decoupling	-6.985	1078.9	0.4110
Recombination	-6.988	1082.8	0.4085
Saha recombination	-7.140	1260.9	0.3184

#### 4.3.3. The optical depth and visibility functions

In Fig. 12, the point where  $\tau \approx 1$  signifies the transitional phase where the universe shifts from an optically dense to an optically thin medium. This is thought to occur close to the time of the last scattering Winther (2024b). We have plotted  $\tau(x)$  and its derivatives in order to compare our model's validity with that of Callin (2006). We have managed to reproduce their results for both Fig. 12 and Fig.13, indicating that our model is of the same level of accuracy as that of Callin (2006).

The decrease of the optical depth  $\tau(x)$  below one signifies the transition of the universe from being optically thick to thin. This transition is closely aligned with the peak of the visibility function  $\tilde{g}(x)$ , marking the epoch when photons began travel-

## The visibility function $\tilde{g}(x)$ and its derivatives

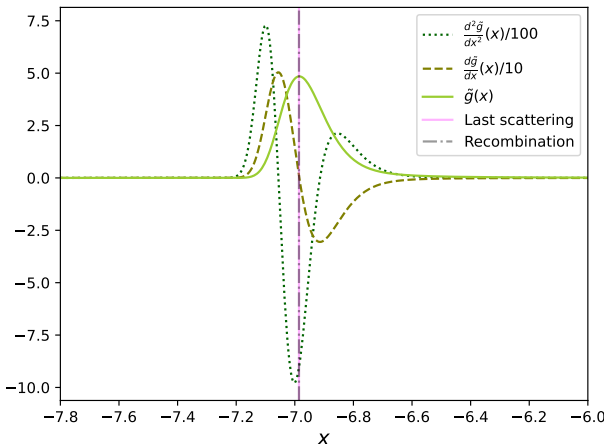


**Fig. 13.** The visibility function  $\tilde{g}(x)$  and its derivatives as a function of  $x$ . The derivatives are scaled to facilitate easier plotting. The pink line marks the peak of  $\tilde{g}(x)$ , and the time most likely for most of the photons to have gone through the last scattering. The gray dashed line marks the time in our model when recombination is likely to have started, when  $X_e < 0.1$ .

ing freely through the universe. The timing of  $\tau(x)$  becoming less than one allows for the identification of when photons in the CMB were last scattered.

The width of the peak in the visibility function  $\tilde{g}(x)$ , Fig. 13, indicates the temporal spread over which photons were last scattered. A wider peak suggests a more extended period of photon interaction with matter, while a narrower peak indicates a more abrupt cessation of scattering. The peak of our visibility function is quite wide, close to  $\Delta x = 0.4$ . This provides insights into the duration and variability of the photon decoupling process, underscoring what we previously have stated; that the last scattering was not a specific time point but rather a period of time when most photons likely scattered for the last time.

It is worth noting that we have ignored the contribution of reionization and helium in this section of our investigation. Omitting these factors do not greatly affect the correctness of our results, however, it does hinder us from studying the effect of the Reionization era, which is an important era in cosmological history. Noting the simplifications we make are necessary when judging the validity of our results. As we have seen here, so far, our results closely resemble that of Callin (2006), whose results we have used to verify our own. From this we conclude that we are ready to expand our project.

## 5. Perturbations

For this section of our investigation we will compute a system of linearized Einstein-Boltzmann equations for photons, baryons, and cold dark matter (CDM), with small perturbations in a Friedman-Lemaître-Robertson-Walker (FLRW) metric. We will numerically compute this system of equations in Fourier space over  $k$  modes, and in our time scale  $x = \ln a$ , observing how several quantities change over time and modes, and comparing our results to that of Callin (2006).

The quantities we are interested in are the dark matter- and baryon density perturbations, given as  $\delta_{CDM}$  and  $\delta_b$ , respectively, the radial velocity ( $v_{CDM}$  and  $v_b$ ) of the two induced by the den-

sity perturbations, and, the gravitational potentials (our metric perturbations)  $\Phi$  and  $\Psi$ .

Lastly, we want to observe the photon multipoles,  $\Theta_\ell(x, t)$ , which in real space describe the distribution photons around a given point  $x$  at a time  $t$ , where  $\Theta_0$  is the mean temperature over all directions of the photons.

This section builds upon our models of the background cosmology of the universe, made in Sections 3 and 4 of this investigation. Like all other sections, we will implement the same equations as Callin (2006) and compare our results to theirs.

### 5.1. Theory

The Einstein-Boltzmann equation system is a series of ordinary differential equations (ODEs) derived by applying the Einstein equations on perturbed Boltzmann equations for photon and matter distribution. The result gives us a system of ODEs describing the behavior of photons, baryons, CDM and the metric. In this section of our investigation we will only provide select explanations deemed necessary to provide context for what we want to achieve. Our implementation relies on the work of Callin (2006). As well, our explanations rely on the work of Winther (2024b), Baumann (2021) and Callin (2006). Unless otherwise stated, it can be assumed that our theoretical basis is retrieved from Winther (2024b).

#### 5.1.1. The perturbed FLRW metric

In our model, the gravitational potentials  $\Phi$  and  $\Psi$  are represented in the perturbations to our FLRW metric.

A perturbed FLRW metric,  $g_{\mu\nu}$ , can in general terms be written as

$$g_{\mu\nu} = \bar{g}_{\mu\nu} + \delta g_{\mu\nu}, \quad (45)$$

where  $\bar{g}_{\mu\nu}$  is the smooth metric and  $\delta g_{\mu\nu}$  is the perturbation. The metric perturbations are coupled to the perturbations in the matter distribution

We use a Newtonian gauge. Writing the perturbed FLRW metric as is done in Callin (2006) we have

$$g_{\mu\nu} = \begin{pmatrix} -(1+2\Psi) & 0 \\ 0 & a^2 \delta_{ij} (1+2\Phi), \end{pmatrix} \quad (46)$$

where  $a$  is the scale factor like before,  $\delta_{ij}$  is the dirac delta function,  $\Phi$  and  $\Psi$  are defined in Eqs(57) and (58), respectively.

#### 5.1.2. Photon multipoles

Experiments measuring the Cosmic Microwave Bakground (CMB) radiation measure the temperature of the photons as functions of their direction in our sky. The statistical properties of the CMB photons can be described through multipoles,  $\Theta_\ell$ , of the photon temperature.

The term  $\ell$  is called the multipole moment. For  $\ell = 0$  we get the monopole,  $\Theta_0$ , which is the average CMB photon temperature over all directions. For  $\ell = 1$ , the dipole,  $\Theta_1$ , is given by the velocity of the fluid, which is an order of magnitude  $10^3$  smaller than the monopole.

Beyond  $\ell = 1$ , we have other anisotropies of the CMB photon temperature, which are 100 times smaller than the dipole. These are what we wish to predict in our numerical model.

The multipoles  $\Theta_\ell$ , for  $\ell > 0$  can in real space be described as

$$\Theta(\mathbf{r}, \hat{\mathbf{p}}, t) = \sum_{\ell=1}^{\infty} \sum_{m=-\ell}^{\ell} a_{\ell m}(\mathbf{r}, t) Y_{\ell m}(\hat{\mathbf{p}}), \quad (47)$$

where  $\mathbf{r}$  is the observer position,  $\hat{\mathbf{p}}$  denotes the propagation direction, and  $t$  is time.  $Y_{\ell m}$  is the spherical harmonics term, which describes the shape of the CMB temperature statistics as our observations are mapped in a unit sphere. The term  $a_{\ell m}$  are the coefficients of the spherical harmonics term.

In our numerical model, we will use  $\Theta_0$ ,  $\Theta_1$ ,  $\Theta_2$ , and  $\Theta_\ell$  as initial conditions for our computations. See implementations in Section 5.2.

### 5.1.3. Perturbation equations

We will numerically compute the linearized Einstein-Boltzmann equation without considering polarization or neutrinos. The equations that we will be solving numerically are the following. The primes indicate derivatives,  $\frac{d}{dx}$ , of our time variable  $x$ .

Starting with the CDM and baryon perturbations we have that

$$\delta'_{\text{CDM}} = \frac{ck}{\mathcal{H}} v_{\text{CDM}} - 3\Phi' \quad (48)$$

$$v'_{\text{CDM}} = -v_{\text{CDM}} - \frac{ck}{\mathcal{H}} \Psi \quad (49)$$

$$\delta'_b = \frac{ck}{\mathcal{H}} v_b - 3\Phi' \quad (50)$$

$$v'_b = -v_b - \frac{ck}{\mathcal{H}} \Psi + \tau' R(3\Theta_1 + v_b), \quad (51)$$

where  $k$  is the current mode of Fourier space we are in,  $c$  is the speed of light,  $\mathcal{H}$  is as previously defined  $aH$ ,  $R = \frac{4\Omega_{\gamma 0}}{3\Omega_{b0}a}$ , and  $v_b$  is the velocity of the density perturbation of barayonic matter  $\delta_b$ . Similarly,  $v_{\text{CDM}}$  is the velocity of the density perturbation of the CDM  $\delta_{\text{CDM}}$ .  $\Phi$  and  $\Psi$  are defined in Eqs(57) and (58), respectively.

In the photon perturbations we get the following:

$$\Theta'_0 = -\frac{ck}{\mathcal{H}} \Theta_1 - \Phi', \quad (52)$$

$$\Theta'_1 = \frac{ck}{3\mathcal{H}} \Theta_0 - \frac{2ck}{3\mathcal{H}} \Theta_2 + \frac{ck}{3\mathcal{H}} \Psi + \tau' \left[ \Theta_1 + \frac{1}{3} v_b \right], \quad (53)$$

$$\begin{aligned} \Theta'_\ell &= \frac{\ell ck}{(2\ell+1)\mathcal{H}} \Theta_{\ell-1} - \frac{(\ell+1)ck}{(2\ell+1)\mathcal{H}} \Theta_{\ell+1} \\ &+ \tau' \left[ \Theta_\ell - \frac{1}{10} \Pi \delta_{\ell,2} \right], \quad 2 \leq \ell < \ell_{\max} \end{aligned} \quad (54)$$

$$\Theta'_\ell = \frac{ck}{\mathcal{H}} \Theta_{\ell-1} - c \frac{\ell+1}{\mathcal{H} \eta(x)} \Theta_\ell + \tau' \Theta_\ell, \quad \ell = \ell_{\max}, \quad (55)$$

where  $\Pi = \Theta_2$  since we are neglecting polarization in our model,  $\delta_{\ell,2}$  is the dirac deltafunction, and  $\tau'$  is the  $x$  derivative of the optical depth  $\tau$ , which is discussed in Section 4.1.1. As mentioned in Callin (2006), the perturbations to the photons represent relative variance in its temperature. See Section 5.1.2 for more.

Finally, the gravitational potentials in our system of equations are given as

$$\begin{aligned} \Phi' &= \Psi - \frac{c^2 k^2}{3\mathcal{H}^2} \Phi + \frac{H_0^2}{2\mathcal{H}^2} [\Omega_{\text{CDM}0} a^{-1} \delta_{\text{CDM}} \\ &+ \Omega_{b0} a^{-1} \delta_b + 4\Omega_{\gamma 0} a^{-2} \Theta_0 + 4\Omega_{\nu 0} a^{-2} N_0] \end{aligned} \quad (57)$$

$$\Psi = -\Phi - \frac{12H_0^2}{c^2 k^2 a^2} [\Omega_{\gamma 0} \Theta_2 + \Omega_{\nu 0} N_2]. \quad (58)$$

As described in Baumann (2021), p.92,  $\Phi'$  has the physical explanation of being the density changes caused by perturbations to the local expansion rate. Its expression is the Possion equation of  $\Phi$ .  $\Psi$  is derived from the expression of anisotropic stress,  $\Psi + \Phi$ .

### 5.1.4. Tight coupling regime

In the tight coupling regime, photons and baryons were tightly coupled. This made space an optically dense medium where the free movement of photons were inhibited, Section 4.1. Due to the tight coupling regime,  $\tau$  becomes very large, and so does  $\tau'$ .

This poses a numerical problem in our ODE system. In the tight coupling regime  $\tau'$  is very large while  $(3\Theta_1 + v_b)$  is very small. The multiplication of a very large and a very small number, such as in Eq.(51), leads to numerical errors. Due to this, we need to make accomodations to our system of equations.

This involves changing the way we define  $\Theta'_1$  and  $v'_b$ . The result of this is seen below.

$$q = \frac{q_1}{q_2} \quad (59)$$

$$\begin{aligned} q_1 &= -[(1-R)\tau' + (1+R)\tau''](3\Theta_1 + v_b) - \frac{ck}{\mathcal{H}} \Psi \\ &+ (1 - \frac{\mathcal{H}'}{\mathcal{H}}) \frac{ck}{\mathcal{H}} (-\Theta_0 + 2\Theta_2) - \frac{ck}{\mathcal{H}} \Theta'_0 \end{aligned} \quad (60)$$

$$q_2 = (1+R)\tau' + \frac{\mathcal{H}'}{\mathcal{H}} - 1 \quad (61)$$

$$v'_b = \frac{1}{1+R} \left[ -v_b - \frac{ck}{\mathcal{H}} \Psi + R(q + \frac{ck}{\mathcal{H}} (-\Theta_0 + 2\Theta_2) - \frac{ck}{\mathcal{H}} \Psi) \right] \quad (62)$$

$$\Theta'_1 = \frac{1}{3}(q - v'_b) \quad (63)$$

### 5.1.5. Initial conditions

The initial conditions of our system of equations are the following,

$$\Psi = -\frac{1}{\frac{3}{2}} \quad (64)$$

$$\Phi = -(1)\Psi \quad (65)$$

$$\delta_{\text{CDM}} = \delta_b = -\frac{3}{2}\Psi \quad (66)$$

$$v_{\text{CDM}} = v_b = -\frac{ck}{2\mathcal{H}}\Psi \quad (67)$$

For the photons:

$$\Theta_0 = -\frac{1}{2}\Psi \quad (68)$$

$$\Theta_1 = +\frac{ck}{6\mathcal{H}}\Psi \quad (69)$$

$$\Theta_2 = -\frac{20ck}{45\mathcal{H}\tau'}\Theta_1 \quad (70)$$

$$\Theta_\ell = -\frac{\ell}{2\ell+1}\frac{ck}{\mathcal{H}\tau'}\Theta_{\ell-1}. \quad (71)$$

$$(72)$$

$$(73)$$

We have set  $\Phi = 1$ . This normalizes the system with respect to  $\Phi$ , and ensures that the curvature perturbations at the initial time is 1.

### 5.2. Implementation details

Like we have done previously, we implemented Runge-Kutta 4 ODE solvers to integrate, and created cubic splines of the solutions and the time  $x$ . This time we splined the solutions with both  $x$  and  $k$ .

We created a  $k$  array with logarithmic spacing starting from  $k_{\min} = 0.5 \cdot 10^{-4} \text{ Mpc}^{-1}$  to  $k_{\max} = 0.3 \text{ Mpc}^{-1}$ . Our time array  $x$  is defined similarly as in the previous sections,  $x \in [-18, 0]$ . The number of points in the arrays can be customized to fit own needs, however, we chose  $n_k = 100$  and  $n_x = 1000$  for the  $k$ - and  $x$ -array respectively.

Having the basics set up, we set up the right hand side of the ODEs for both the full system and the tight coupling regime, described in Sections 5.1.3 and 5.1.4. We also set the initial conditions, as described in 5.1.5.

After having solved and splined the solutions to the ODEs, we make our plots.

Note, we only compute the multipoles up to  $\ell = 6$  to derive the results of this section.

#### 5.2.1. Tight coupling regime

We define the tight coupling regime similarly to that of Callin (2006), which has defined the regime to be before Recombination (we set this as  $x = -8.3$ ) with  $\tau' > 10$  and  $\frac{ck}{\mathcal{H}} < \frac{1}{10}$ .

While in this regime we only evolve the ODEs of  $\Theta'_0$  and  $\Theta'_1$ .

We get the time of tight coupling when we run this for each  $k$  mode, and switch to our full system when we have hit the tight coupling time,  $x_{tc}$ , for that mode.

### 5.3. Results

The discussion of our results focus mainly on the attempting to produce a chronological narration of the evolution of our uni-

verse from the radiation dominated period until today. The figures represented are sectioned into three eras: the radiation dominated era (yellow), the matter dominated era (blue), and the dark energy dominated era (magenta). We emphasize an interpretation based off of our results, and will point to them in our discussion. Our results are computed for three  $k$  modes that are  $k = 0.001$ ,  $k = 0.01$  and  $k = 0.1$  in units of  $\text{Mpc}^{-1}$ .

**Plot of density perturbations  $|\delta_{\text{CDM}}|$ ,  $|\delta_b|$ ,  $|\delta_\gamma|$**

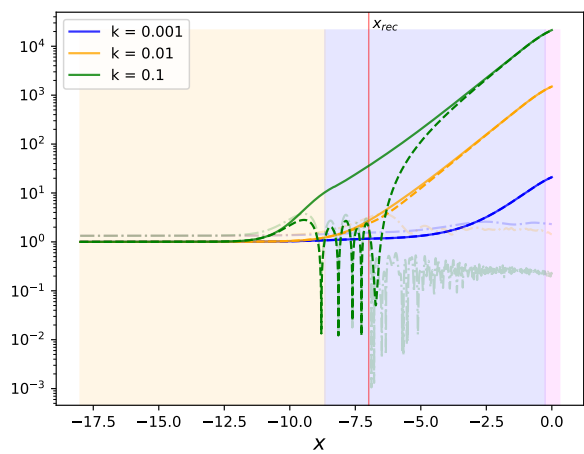


**Fig. 14.** Plot of the absolute values of the density perturbation for  $\delta_{\text{CDM}}$ ,  $\delta_b$  and  $\delta_\gamma$  for different modes  $k$ . The density perturbation of CDM are represented by a solid line, while the dashed lines are for baryons.  $\delta_\gamma$  is shown in faint lines, only for comparison to the density perturbations of CDM and baryons. See Fig.(16) for a better plot of  $\delta_\gamma$ . The yellow region indicates the radiation dominated era, the blue region indicates the matter dominated era, and the magenta region indicates the dark energy dominated era. Recombination time is marked with a red vertical line.

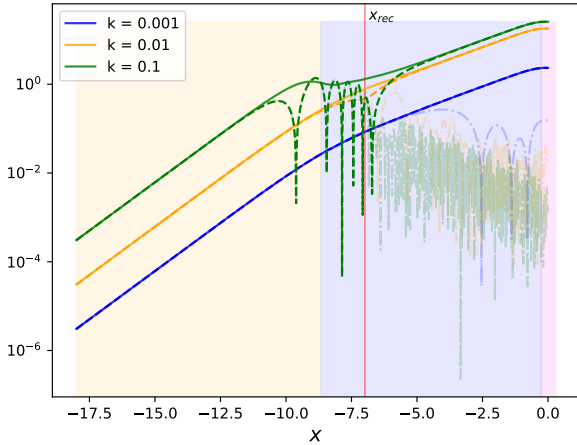
#### 5.3.1. Radiation dominated era

Initially, the universe was extremely hot and dense, forming a tightly coupled photon-baryon fluid. The gravitational potentials  $\Phi$  and  $\Psi$  were mainly sourced from the density perturbation of radiation,  $\delta_\gamma$ , and the density parameter  $\Omega_\gamma(a)$ .

In Fig.(14), density perturbations for cold dark matter (CDM), baryons, and photons are plotted. Early in the radiation era, these perturbations track closely, with radiation's influence being predominant.

The density fluctuations in the photon-baryon fluid are stabilized by the radiation pressure in the very early times of the radiation dominated era. Radiation pressure counteracts gravity, stabilizing perturbation fluctuations and preventing significant clustering in radiation.

As time progresses, the density perturbations of CDM and baryons begin to grow. Gravity attempts to compress the fluid into potential wells. However, the radiation pressure of the photons push back, causing oscillations in the density perturbations of the photon-baryon fluid. These oscillations are known as acoustic oscillations, and are evident in Fig.(14), where we see that the perturbations in the CDM and baryons no longer grow at the same rate, but that the  $\delta_b$  starts decreases before it starts to oscillate. This is process, where the photon radiation opposes gravity, and in the process causes oscillations in the density perturbations is called *radiation driving*. Hu (2001)

**Plot of perturbation velocities  $|v_{CDM}|, |v_b|, |v_\gamma|$** 

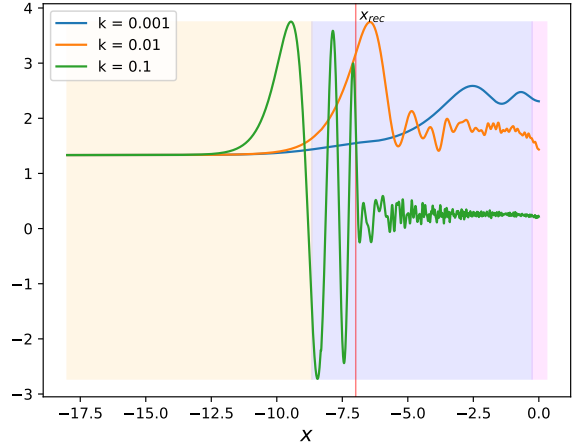
**Fig. 15.** Plot of the absolute values of the perturbation velocities for  $v_{CDM}$ ,  $v_b$  and  $v_\gamma$  for different modes  $k$ . The perturbation velocities of CDM are represented by a solid line, while the dashed lines are for baryons.  $v_\gamma$  is shown in faint lines, only for comparison to the perturbation velocities of CDM and baryons. See Fig.(17) for a better plot of  $v_\gamma$ . The yellow region indicates the radiation dominated era, the blue region indicates the matter dominated era, and the magenta region indicates the dark energy dominated era. Recombination time is marked with a red vertical line.

In Fig.(15) we have plotted the velocities of the perturbations plotted in Fig.(14). Here as well, we see that the velocity of the perturbations behave similarly for CDM, baryons and photons in the very early times. We observe that as the matter perturbations grow, the velocity of the perturbations of the baryon-photon fluid also start to oscillate. The velocities of the baryon and photon perturbation before decoupling, i.e. before  $x_{rec}$ , are indicative of the motion of the photon-baryon fluid within potential wells. A decrease in velocity suggests that the radiation is losing its kinetic energy due to expansion and the decreasing influence of radiation pressure. Likewise, an increase suggests that the fluid is climbing out of the potential well as the radiation pressure from the photons opposes gravity.

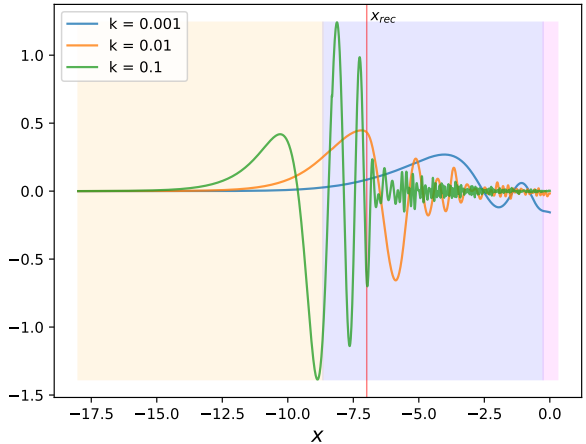
**Discussion of gravitational potentials:** Fig.(18) shows that  $\Phi$  decreases when the velocity of photon and baryon perturbations,  $v_\gamma$  and  $v_b$ , begin to oscillate. This more rapid decrease on smaller scales ( $k = 0.1$ ) suggests that radiation pressure significantly influences these gravitational potentials. A decrease in  $\Phi$  indicates decrease in depth of the gravitational well. Early in the radiation dominated era we see that  $\Phi + \Psi = 0$ , indicating that the photon-baryon fluid behaves as a perfect fluid without anisotropic stress. As we move into the matter dominated era, the influence of anisotropic stress becomes more pronounced.

### 5.3.2. Matter dominated era and recombination

As the universe continues to expand and cool,  $\Omega_m$  increases as we enter the matter dominated era. In this era, gravitational forces start to overcome the force of radiation pressure, allowing perturbations in baryons to grow which leads to structure formation. The density parameters  $\Omega_{CDM}$ ,  $\Omega_b$ , and the density perturbations  $\delta_{CDM}$ ,  $\delta_b$ , drive the gravitational potentials  $\Phi$  and  $\Psi$ . The density parameters and density perturbations of radiation still affect the gravitational potentials, but are no longer the driving factors.

**Plot of  $\delta_\gamma = 4\Theta_0$** 

**Fig. 16.** Plot of density of radiation perturbation for different  $k$  modes. The yellow region indicates the radiation dominated era, the blue region indicates the matter dominated era, and the magenta region indicates the dark energy dominated era. Recombination time is marked with a red vertical line.

**Plot of  $v_\gamma = -3\Theta_1$** 

**Fig. 17.** Plot of velocity of radiation perturbation for different  $k$  modes. The yellow region indicates the radiation dominated era, the blue region indicates the matter dominated era, and the magenta region indicates the dark energy dominated era. Recombination time is marked with a red vertical line.

In the early matter dominated era, the velocity of the perturbations of the baryons,  $v_b$ , oscillate with the velocity perturbation of photons  $v_\gamma$  up until the time of recombination. Around this time, the photons and baryons decouple. The density perturbations of the photons continue oscillating after recombination, as seen in Fig.(14) and (16). Eventually their energy dissipates, and the velocity of the perturbations decreases, as seen in Fig.(17).

In the previous section we calculated the sound horizon to be about 163.81 Mpc. The sound horizon is the maximum distance the acoustic waves could have traveled in the photon-baryon fluid from the beginning of the universe until the time of recombination. The sound horizon then, also represents the scale of the largest perturbation of the density of baryons and photons. This

scale should be seen as the first peak in the angular CMB power spectrum, which we will compute in the next section.

**Discussion of gravitational potentials:** In the matter dominated era, the anisotropic stress,  $\Psi + \Phi$ , starts to increase, see Fig.(19). The increase is quicker for small scales  $k$ . Around  $x_{rec}$  anisotropic stress has increased in for all the scales we observe, peaking a little after for large scales  $k = 0.001$ , indicating that the decoupling of the baryons and photons. We note that in the smallest scale  $k = 0.1$ , the anisotropic stress only slightly deviates from the behaviour of a perfect fluid, and returns eventually. This is, we believe, is likely due to the decrease in  $v_\gamma$  around this time, Fig.(17), as the oscillation of  $\delta_\gamma$  slows down, Fig.(16). Since the photon perturbations don't cluster like matter perturbations, most of the photon density perturbations are in the small scale  $k = 0.1$ , and we observe their effect on the anisotropic stress in Fig.(19).

**Plot of  $\Phi$**

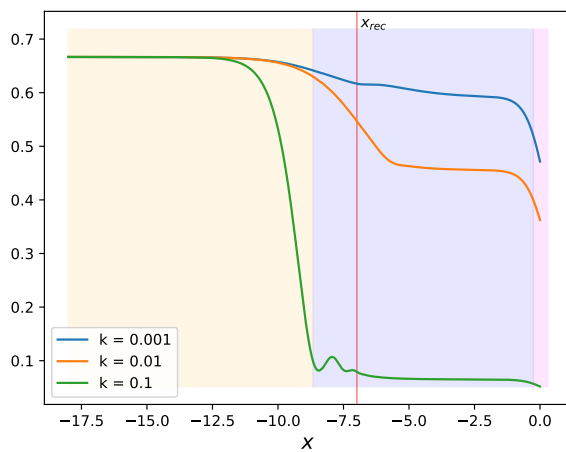


**Fig. 18.** Plot of  $\Phi$  for different  $k$  modes. The yellow region indicates the radiation dominated era, the blue region indicates the matter dominated era, and the magenta region indicates the dark energy dominated era. Recombination time is marked with a red vertical line.

### 5.3.3. The Multipoles

**Monopole  $\Theta_0$ :** The monopole term  $\Theta_0$ , represents the average temperature of the CMB, and is directly tied to the density perturbations of photons,  $\delta_\gamma = 4\Theta_0$ . It is the most dominant term of the multipoles. During the late radiation-dominated era, the monopole shows significant oscillations, which are due to the photon-baryon fluid opposing gravitational forces with radiation pressure, in Fig.(20).

**Dipole  $\Theta_1$ :** The dipole term  $\Theta_1$  is associated with the velocity of the photon-baryon fluid before decoupling. In the early universe, late radiation dominated era, as the baryon-photon fluid oscillates within potential wells, the dipole moment oscillates correspondingly, reflecting the kinetic aspect of these fluctuations. We note that the dipole defines the velocity of the photon perturbations,  $v_\gamma = -3\Theta_1$ . Fig.(21) the oscillations, which diminish as after  $x_{rec}$ , due to the decoupling of photons and baryons. From Fig.(21) and (17), we can interpret the velocity of the photon perturbations as decreasing after photon decoupling. This, shows the diminishing of radiation driving, meaning the photon perturbation velocity dissipates as it no longer opposing gravitational forces to the same effect as before.

**Plot of anisotropic stress  $\Phi + \Psi$**

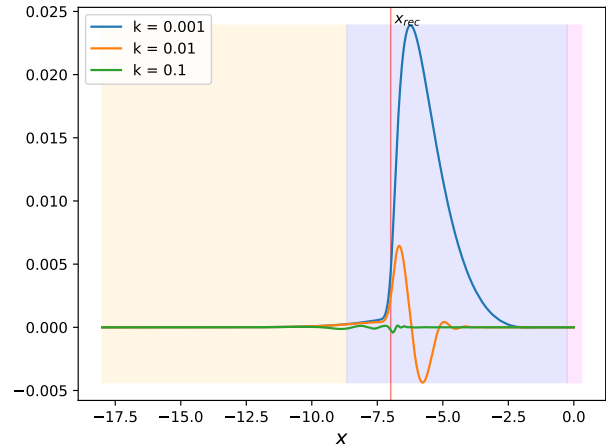


**Fig. 19.** Plot of anisotropic stress,  $\Phi + \Psi$  for different  $k$  modes. The yellow region indicates the radiation dominated era, the blue region indicates the matter dominated era, and the magenta region indicates the dark energy dominated era. Recombination time is marked with a red vertical line.

**Plot of  $\Theta_0$**

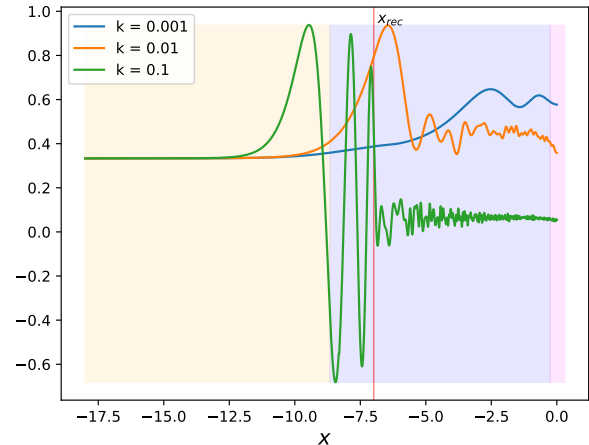


**Fig. 20.** Plot of  $\Theta_0$  for different  $k$  modes. The yellow region indicates the radiation dominated era, the blue region indicates the matter dominated era, and the magenta region indicates the dark energy dominated era. Recombination time is marked with a red vertical line.

**Quadrupole  $\Theta_2$ :** The quadrupole term  $\Theta_2$  is the term related to the polarization of the photons. During tight coupling this term is close to zero, but when the local distribution of photons deviates from spherical symmetry it becomes significant. Such as during the last scattering surface. In Fig.(22) we observe  $\Theta_2$  deviating from zero around the time of recombination  $x_{rec}$ . Photons are freed after recombination the quadrupole becomes more pronounced.

## 6. The Power Spectra

So far, we have computed the background geometry of the universe, its ionization history, and the evolution of structure growth in the universe. We are now ready to move on to our final goal;

### Plot of $\Theta_1$

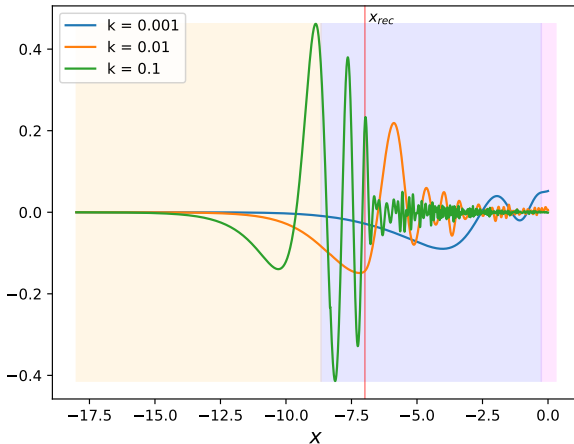


**Fig. 21.** Plot of  $\Theta_1$  for different  $k$  modes. The yellow region indicates the radiation dominated era, the blue region indicates the matter dominated era, and the magenta region indicates the dark energy dominated era. Recombination time is marked with a red vertical line.

### Plot of $\Theta_2$

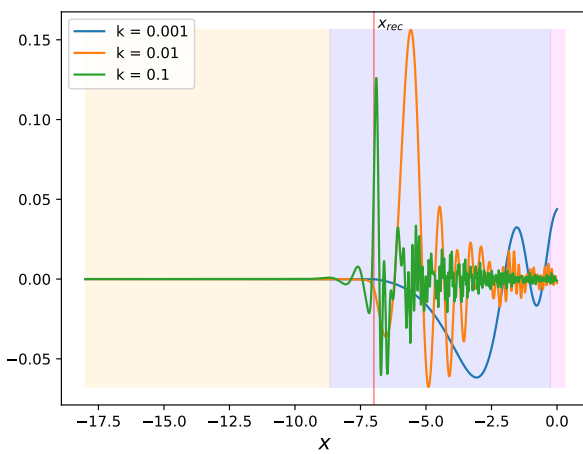


**Fig. 22.** Plot of  $\Theta_2$  for different  $k$  modes. The yellow region indicates the radiation dominated era, the blue region indicates the matter dominated era, and the magenta region indicates the dark energy dominated era. Recombination time is marked with a red vertical line.

computing the CMB angular power spectrum and the matter power spectrum.

In this last chapter of our investigation, we will focus on computing the last spectra, using what we have established so far.

We establish a concise theory, meant to give a broad overview of the physics behind our final computations. After this we have given a brief overview of our implementation, we present and discuss our main results. We compare our results of the CMB power spectrum with the Planck spectrum low  $\ell$  TT data. In the end we conclude our project with final remarks.

## 6.1. Theory

For this section of our investigation, we will give a quick introduction to the most essential physics needed to compute and interpret our final results.

### 6.1.1. Matter power spectrum

The matter power spectrum quantifies the distribution of matter density in our universe over scales  $k$ . With smaller  $ks$  represent larger structures and larger  $ks$  representing smaller structures. The matter power spectrum is dictated by the primordial power spectrum and how the modes of scale relate to each other.

In our model we have normalized the initial curvature perturbations to 1, and define the matter power spectrum  $P(k, x)$  as

$$P(k, x) = |\Delta_M(k, x)|^2 P_{\text{primordial}}(k), \quad (74)$$

where

$$\Delta_M(k, x) \equiv \frac{c^2 k^2 \Phi(k, x)}{\frac{3}{2} \Omega_{M0} a^{-1} H_0^2}$$

is the matter over-density field, and  $P_{\text{primordial}}(k)$  is the matter power spectrum

It is useful to note that the primordial power spectrum is related to the primordial amplitude,  $A_s$ , as

$$P_{\text{primordial}}(k) = \frac{2\pi^2}{k^3} A_s \left( \frac{k}{k_{\text{pivot}}} \right)^{n_s - 1}, \quad (75)$$

where  $k_{\text{pivot}}$  is the  $k$  for when  $P(k) = 1$ , and  $n_s$  is the spectral index.

We define the equality scale,  $k_{eq}$  as

$$k_{eq} = \frac{a_{eq} H(a_{eq})}{c} = \frac{\mathcal{H}(x_{eq})}{c}, \quad (76)$$

where  $a_{eq}$  is the scale factor for the time,  $x_{eq}$ , of matter-radiation equality.

### 6.1.2. Angular power spectrum

From Section 5.1.2, we remember the expansion of the photon multipoles in real space,  $\Theta_\ell$ , to be

$$\Theta(\mathbf{r}, \hat{p}, t) = \sum_{\ell=1}^{\infty} \sum_{m=-\ell}^{\ell} a_{\ell m}(\mathbf{r}, t) Y_{\ell m}(\hat{p}). \quad (77)$$

The term  $a_{\ell m}$  are the coefficients of the spherical harmonics term  $Y_{\ell m}(\hat{p})$ .

The temperature field of the CMB spectrum in spherical harmonics form is given by

$$T(\hat{n}) = \sum_{\ell m} a_{\ell m} Y_{\ell m}(\hat{n}). \quad (78)$$

The CMB power spectrum,  $C_\ell$ , is defined as the expectation value of  $|a_{\ell m}|^2$ ,

$$C_\ell \equiv \langle |a_{\ell m}|^2 \rangle = \langle a_{\ell m} a_{\ell m}^* \rangle. \quad (79)$$

In order to calculate the CMB up spectrum, we need to find the temperature field,  $T(\hat{n})$ , today. In the previous section, we computed the evolution of the  $\Theta_\ell$  multipoles up until  $\ell = 6$  in

Fourier Space. In order to find the temperature field today, we would need to compute our multipoles up to  $\ell \approx 1200$ .

However, this is a tedious, and potentially computationally expensive, process. Our solution to this problem is the Line of Sight (LOS) integration, see Section 6.1.3.

We compute the  $C_\ell$ s using the following expression

$$C_\ell = 4\pi \int_0^\infty A_s \left( \frac{k}{k_{\text{pivot}}} \right)^{n_s-1} \Theta_\ell(k)^2 \frac{dk}{k}, \quad (80)$$

where  $\Theta_\ell$  is computed from the LOS method.

### 6.1.3. Line of sight integration

The Line of Sight (LOS) integration is a method developed by Zaldarriaga and Seljak, Seljak & Zaldarriaga (1996). The LOS narrows down to the following expression:

$$\Theta_\ell(k, x=0) = \int_{-\infty}^0 \tilde{S}(k, x) j_\ell[k(\eta_0 - \eta)] dx, \quad (81)$$

where  $k$  are Fourier modes corresponding to scales of size in terms of wavenumber, which is inversely proportional to the real-space size of a given perturbation. The term  $j_\ell[k(\eta_0 - \eta)]$  is the spherical Bessel function, which accounts for the spherical projection of the 3D field onto a 2D sphere. The term  $\tilde{S}(k, x)$ , is the source function, which describes the combined influences of temperature fluctuations, gravitational potential shifts, Doppler shift of the fluid and polarization effects on the Cosmic Microwave Background (CMB) anisotropies, See Eq.(82).

We compute the source function in our project, given by

$$\begin{aligned} \tilde{S}(k, x) = & \tilde{g} \left[ \Theta_0 + \Psi + \frac{1}{4} \Pi \right] + e^{-\tau} [\Psi' - \Phi'] \\ & - \frac{1}{ck} \frac{d}{dx} (\mathcal{H} \tilde{g} v_b) + \frac{3}{4c^2 k^2} \frac{d}{dx} \left[ \mathcal{H} \frac{d}{dx} (\mathcal{H} \tilde{g} \Pi) \right], \end{aligned} \quad (82)$$

where we have that  $\Pi = \Theta_2 + \Theta_0^P + \Theta_2^P$ . Because we ignore the contribution of polarization we set  $\Theta_0^P = \Theta_2^P = 0$ , giving  $\Pi = \Theta_2$ .

The physical intuition behind the first term in the source function, known as the Sachs-Wolfe (SW) term, is that the CMB radiation we observe in a given direction on the sky is in essence the integral of the local CMB monopole,  $\Theta_0$ , along the line of sight from us to infinity. This is the most dominant term, and conveys that the CMB anisotropies we observe today come from temperature inhomogeneities that were present at recombination which froze in when the Universe became transparent.

The other terms are correction terms. The second term is the Integrated Sachs-Wolfe (ISW) term, which encapsulates the variations in gravitational potentials encountered by photons. The third term is a Doppler term, as it describes the shift in velocity of the photon-baryon fluid perturbations, that can be observed if the fluid climbs in and out of potential wells which change with time. The last term addresses the polarization of the light.

When performing the LOS integration numerically, we integrate the derivative of  $\Theta_\ell$  with respect to  $x$

$$\frac{d\Theta_\ell(k, x)}{dx} = \tilde{S}(k, x) j_\ell[k(\eta_0 - \eta)]. \quad (83)$$

### 6.2. Implementation details

As done previously, we integrate over a  $k$ -array with logarithmic spacing starting from  $k_{\min} = 0.5 \cdot 10^{-4}$  Mpc $^{-1}$  to  $k_{\max} = 0.3$  Mpc $^{-1}$ , and a linearly spaced  $x$  array.

We created a  $z$ -array with  $dz = 0.05$ , with a starting value of 0 and an endpoint at  $z = k_{\max} \eta_0$ . Where  $\eta_0$  is the conformal time today and  $k_{\max}$  is the last  $k$  value in our  $k$ -array.

When computing the spherical Bessel function for redshifts,  $z$ , we employed a pre-made module created by Winther (2024b) which can be accessed in the Utils file of Winther (2024a), and created a spline of the Bessel function values for redshifts,  $z$ .

We then perform our LOS integration for  $x \in [-8.3, 0]$ , with  $dx = 0.05$  in order to ensure proper resolution in our integration. Our integration starts from  $x = -8.3$  to ensure that we integrate before recombination has started. We compute  $\Theta_\ell(k, x)$  for a selection of 63 different  $\ell$ s from  $\ell = 2$  up to  $\ell = 2000$ .

The numerical integration method we employ to solve the differential equation, Eq.(83), is the trapezoidal method.

Computing the matter power-spectrum is done as described in Section (6.1.1). We set  $A_s = 2.1 \cdot 10^{-9}$ ,  $n_s = 0.965$  and  $k_{\text{pivot}} = 0.05$  Mpc.

### 6.3. Results

The following section will attempt to summarize and interpret the results of this numerical investigation.

#### 6.3.1. CMB power-spectrum

The CMB power spectrum in Fig.(23) was plotted from  $C_\ell$  as defined in Eq.(80), and scaled multiplying  $C_\ell$  with  $\frac{\ell(\ell+1)}{2\pi} 10^6 T_{CMB}^2$ . We have plotted the in blue  $C_\ell$  along with the various terms of the source function, Eq.(82), in red we have the observational low  $\ell$  TT data of the Planck spectrum.

Starting our analysis at the largest scales of the universe, for  $\ell \leq 20$ , observe the Sachs-Wolfe plateau. In the source function, Eq.(82), this term is the dominating term, which can clearly be seen in Fig.(23). In large scales especially, we see that the  $C_\ell$  is dominated by the SW term, where the temperature fluctuations are close to constant for the scales  $\ell \leq 20$ . The red observations follow our numerical model well, with some deviations from the blue line. The initial  $\ell$  terms have high uncertainty due to cosmic invariance, which are inherent uncertainties. Our first check of the last part of our model is complete, the SW plateau is corroborated by observed data.

As we move out from the SW plateau, we observe an increase in the contribution of the Doppler term, indicating an increase in the velocity of the baryons.

Moving on to the first peak, which should be localized around  $\ell \approx 200$ . This appears to be the case in Fig.(23), meaning that our model is adhering to theoretical predictions of a flat universe, as this peak suggests Hu (2001).

The first peak of the CMB power spectrum is the first compression of the sound wave. The height of the peak is affected by baryon loading, the process in which the baryons in the photon-baryon fluid lowers the sound speed, changing the height of the peaks in the  $C_\ell$ , and makes the oscillations asymmetric. The oscillations after the first peak do not appear to be symmetric, indicating that the photon-baryon fluid in our model is affected by baryon loading.

As the scales of size we are looking at get smaller, we observe more rapid oscillations of our CMB power spectrum.

Around the second peak, the Doppler term of the source function is having an increased presence. This indicates that there is a increase in the velocity of the baryons, along with the oscillations in the  $C_\ell$  we can interpret that there is an increase of baryons, and that we are observing the effects of baryon loading.

As we approach the upper end of the scales,  $\ell \geq 800$ , we arrive at the diffusion damping tail of the power spectrum. On these small scales, the photon diffusion washes out the perturbations in the  $C_\ell$ , leading to the effect of the  $C_\ell$  diminishing as the scales become smaller. This part of the  $C_\ell$  is also characterized by an increased relative contribution of the polarization term of the source function, indicating that the photons are scattering or able to move in a less restricted way.

### The angular CMB power spectrum

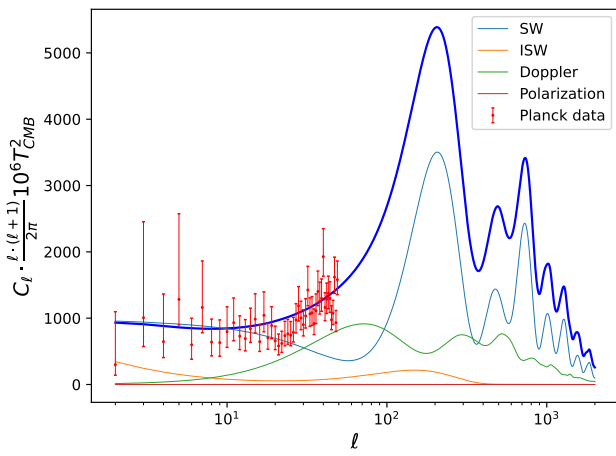


**Fig. 23.** Plot of  $C_\ell$  over "wavelength"  $\ell$  of mode  $k$ .

### 6.3.2. The matter power-spectrum

In Fig.(24), we have plotted the matter power-spectrum, which quantifies the distribution of baryons and CDM for Fourier mode size scales  $k$ . The dotted line in the figure marks the equality scale  $k_{eq}$ , at the time of radiation-matter equality. Perturbations on  $k$  scales smaller than this (physically larger) entered the horizon before matter dominated over radiation, and those on larger scales  $k$  (physically smaller) entered after. This part of the power spectrum shows a close to power-law relation between the size of the perturbations and the structure growth, where  $P(k)$  grows with  $k$ , this is characteristic of the primordial matter power spectrum.Shen (2023)

On the larger  $k$  scales after  $k_{eq}$  we observe oscillations in  $P(k)$ . These are baryonic acoustic oscillations (BAO), caused by the initial oscillations of the photon-baryon fluid, which have perpetuated in the baryonic fluid.

We also observe a suppression of structure growth for the  $k > k_{eq}$ . This is commonly known as the Mezaris effect, it occurs as matter perturbations are unable to grow effectively under the dominant influence of radiation pressure.Shen (2023)

As we have mentioned before, we have neglected to include neutrinos in our model. This in turn affects the height of our peak in Fig.(24), making it lower than what it should be in a more accurate model.

### The matter power spectrum

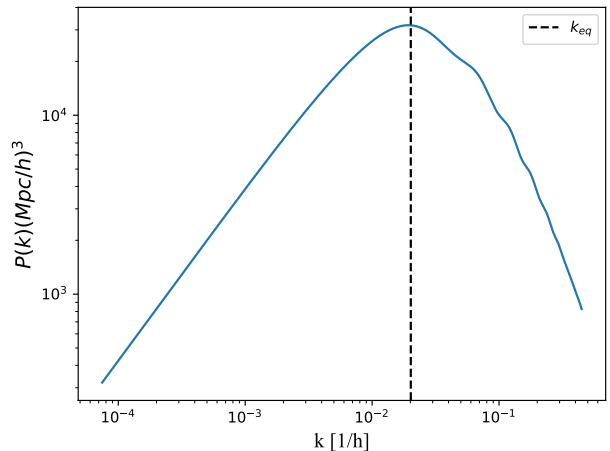


**Fig. 24.** Plot of the matter power spectrum  $P(k)$  over modes  $k$ .

### 6.3.3. Photon multipoles

In Fig.(25) we have plotted the transfer function  $\Theta_\ell(k)^2$ , and in Fig.(26) we have plotted  $\frac{|\Theta_\ell(k)|^2}{k}$ ,the integrand of the  $C_\ell$ . For a select number of  $\ell$ s,  $\ell = [7, 60, 100, 500, 1000]$ .

In Fig.(26), we have marked the peak for each  $\ell$ . This had been done to validate the accuracy of our model as we expect the peaks of  $\frac{|\Theta_\ell(k)|^2}{k}$  to align at  $k\eta_0 \approx \ell$  for each  $\ell$ . We see in the figure that the peaks do in fact align just above this point, which validates our model. However, we note that as the  $\ell$ s increase, our resolution worsens, indicated by less tightly packed oscillations. This we believe suggests that our model becomes less accurate for higher  $\ell$ .

### Plot of $\Theta_\ell(k)^2$

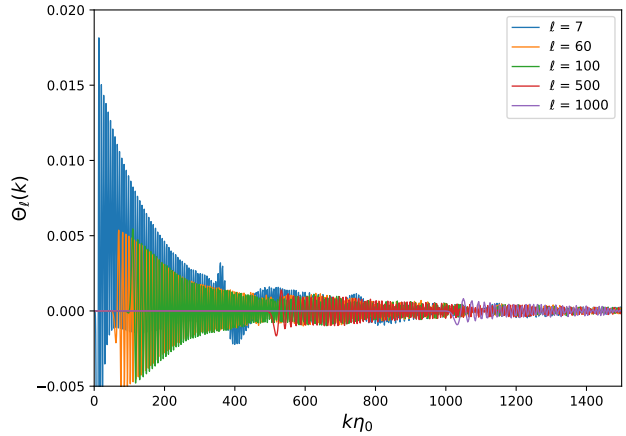


**Fig. 25.** Plot of  $\Theta_\ell(k)^2$ , over modes  $k$  multiplied by conformal time today,  $\eta_0$ . For a select number of  $\ell$ .

## 7. Conclusions

The main goal of our investigation was to compute the CMB power spectrum, and the matter power spectrum. The pursuit of our goal was done under the assumption of fiducial cosmology

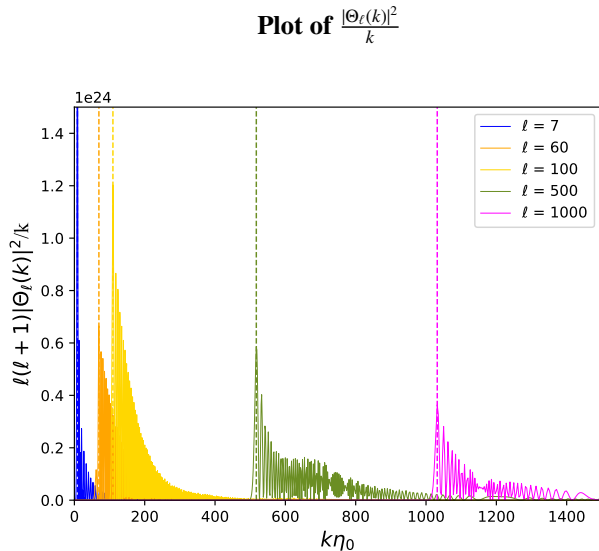


**Fig. 26.** Plot of the integrand of  $C_\ell$ ,  $|\Theta_\ell(k)|^2/k$ , over modes  $k$  multiplied by conformal time today,  $\eta_0$ . For a select number of  $\ell$ ,  $|\Theta_\ell(k)|^2/k$  is scaled by  $\ell(\ell + 1)$

based off of Planck 2018 results, Aghanim et al. (2020), and neglecting the effects of neutrinos, the reionization, and polarization. We achieved our final results by first computing the background evolution of our universe, which involved computing the cosmological geometry, Section 3, and then computing the Recombination Era, see Section 4.

In Section 3, we found that the expansion of our universe starts accelerating at around 7.756 Gyrs, the radiation-matter equality time at 23200 years and the matter-dark energy equality time to be at 10.38 Gyrs in cosmic time, Tab.(2). We also compared our fiducial cosmology model with a model from an MCMC fit based off of observations by Betoule et al. (2014), and found a good fit. However, we still evaluated the original fiducial cosmology to be a better choice when continuing our project, due to the lower level of uncertainty in the data by Aghanim et al. (2020).

In Section 4, we found the time when recombination was most likely to occur to be at cosmic time 0.4085 Myrs, Tab.(4). Our photon decoupling time was found to likely be around the same time at 0.4110 Myrs.

Following this, in Section 5, we computed a set of linearized Einstein-Boltzmann equations, predicting how perturbations in CDM, baryon, and photons behave over the different eras of radiation domination, matter domination and dark energy domination. These behaviours were plotted in Figs.(14, 15, 16, and 17). Additionally, we computed the evolution of the gravitational potential  $\Phi$ , Fig.(18), and the anisotropic stress  $\Phi + \Psi$ , Fig.(19). From these results we were able to infer a rough chronological history of the evolution of perturbation in the universe, which was consistent with our expectations.

Finally, we produced the CMB angular power spectrum and the matter power spectrum. We were able to produce the known characteristics of both spectra. For the CMB power spectrum we observed the Sachs-Wolfe plateau, an initial peak around  $\ell = 200$ , asymmetry in the characteristic acoustic oscillations caused by baryon loading, and the diffusion damping tail.

The reproduced matter power spectrum also contained well-known characteristics like the power-law growth of the primordial power spectrum for  $k < k_{eq}$ , a peak at  $k = k_{eq}$ , BAOs, and the Mezaros effect.

We assumed a flat universe  $\Lambda CDM$  model, which our results corroborated, indicating that our model worked relatively well despite our simplifications.

This judgement is based off of the analysis we have done so far. On a qualitative level, we have deemed our results to be relatively good, as they concur with expected theory in the broad strokes. However, this investigation is still lacking in rigorous quantitative analysis and is at the mercy of its simplifications. This investigation would benefit from a comparison of how the inclusion of neutrinos, polarization and ionization could improve the accuracy of our results, or expose flaws.

Additionally, if given more time, the investigation would have benefited from a comparison of the present model with observations and a statistical analysis, as well as more analytical benchmarks to verify our results. This is especially true of Section 6.

## References

- Aghanim, N., Akrami, Y., Ashdown, M., et al. 2020, *Astronomy & Astrophysics*, 641, A6
- Arendse, N., Agnello, A., & Wojtak, R. J. 2019, *Astronomy & Astrophysics*, 632, A91
- Baumann, D. 2021, *Cosmology*, last accessed: June 7th 2024
- Betoule, M., Kessler, R., Guy, J., et al. 2014, *Astronomy & Astrophysics*, 568, A22
- Callin, P. 2006, *How to Calculate the CMB Spectrum*, 1st edn.
- Crowley, B. & Gregori, G. 2014, *High Energy Density Physics*, 13, 55
- Dodelson, S. 2020, *Modern Cosmology*, 2nd edn. (Academic Press)
- Hu, W. 2001, *Cosmology*, last accessed: June 7th 2024
- Kotlarchyk, M. 1999, *Encyclopedia of Spectroscopy and Spectrometry*, last accessed: 2nd of April 2024
- Page, L., Hinshaw, G., Komatsu, E., et al. 2007, *The Astrophysical Journal Supplement Series*, 170, 335–376
- Reichardt, C. L., Ade, P. A. R., Bock, J. J., et al. 2009, *The Astrophysical Journal*, 694, 1200–1219
- Seljak, U. & Zaldarriaga, M. 1996, *The Astrophysical Journal*, 469, 437
- Shen, S. 2023, *AST4320: Cosmology and Extragalactic Astrophysics Lecture Notes* (Institute of Theoretical Astrophysics, University of Oslo), lecture notes for the course AST4320
- Winther, H. 2024a, *Github page of Hans Winther*, last accessed on June 7, 2024
- Winther, H. 2024b, *Lecture Notes on Cosmology*, Institute of Theoretical Astrophysics, University of Oslo, last accessed on June 7, 2024